Properties of Omp2a-Based Supported Lipid Bilayers: Comparison with Polymeric Bioinspired Membranes

Anna Puiggalí-Jou,[1,2] Jan Pawlowski,[3] Luis J. del Valle,[1,2] Catherine Michaux,[4] Eric A. Perpète,[4] Slawomir Sek,[3,*] and Carlos Alemán[1,2,*]

[1] Departament d'Enginyeria Química, EEBE, Universitat Politècnica de Catalunya, C/ Eduard Maristany, 10-14, Ed. I2, 08019, Barcelona, Spain

[2] Barcelona Research Center for Multiscale Science and Engineering, Universitat Politècnica de Catalunya, C/ Eduard Maristany, 10-14, Ed. C, 08019, Barcelona, Spain

[3] Biological and Chemical Research Centre, Faculty of Chemistry, University of Warsaw, Zwirki i Wigury 101, 02-089 Warsaw, Poland.

[4] Laboratoire de Chimie Physique des Biomolécules, University of Namur, Rue de Bruxelles, 61, 5000 Namur, Belgium

* slasek@chem.uw.edu.pl and carlos.aleman@upc.edu

ABSTRACT

Omp2a β-barrel outer membrane protein has been reconstituted into supported lipid bilayers (SLBs) to compare the nanomechanical properties (elastic modulus, adhesion forces and deformation) and functionality of the resulting bioinspired system with that of Omp2a-based polymeric nanomembranes (NMs). Protein reconstitution into lipid bilayers has been performed using different strategies, the most successful one being consisting into a detergent-mediated process into preformed liposomes. The elastic modulus obtained for the lipid bilayer and Omp2a are ~19 MPa and 10.5 ± 1.7 MPa, respectively. Accordingly, the protein is softer than the lipid bilayer, while the latter exhibits less mechanical strength than polymeric NMs. Besides, the function of Omp2a in the SLB is similar to that observed for Omp2a-based polymeric NMs. Results open the door to hybrid bioinspired substrates based on the integration of Omp2a-proteoliposomes and nanoperforated polymeric free-standing NMs.

INTRODUCTION

Membrane proteins (MPs) play a key role in many biological processes, such as cell recognition, signal transmission, enzymatic reactions, and transport of metabolites.[1-3] Their importance is proved by the fact that 50% of medical drugs currently on the marked target MPs.[2-4] The structure of MPs is restricted to α-helix and β-barrel due to the need to satisfy all hydrogen bonds within the water-excluded native bilayer environment. Although α-helical MPs are present in most biological membranes, β-barrel MPs are exclusively found in the outer membranes (OM) of Gram-negative bacteria[5] and eukaryotic organelles directly derived from prokaryotic ancestors namely, mitochondria[6] and chloroplasts.[7]

Porins are β-barrel outer membrane proteins (OMPs) that form water-filled open channels and allow the passive penetration of hydrophilic molecules. Due to their capacity in exchange of ions and small nutrients (i.e. typically < 667 Da) over the OM, porins have been used to fabricate smart biomimetic nanomembranes (NMs) that could incorporate biological functions, such as controlled ion transport.[8] For this purpose, three different approaches are currently followed: 1) re-constitution of natural OMPs into lipid bilayers;[9,10] 2) immobilization of porins onto supported organic or inorganic NMs;[11-14] and 3) confinement of OMPs inside synthetic pores.[15-17] In recent studies, we have probed the technological potential of approaches 2) and 3) coupling Omp2a, a β-barrel OMP from Brucella melitensis that permits the passive diffusion of small molecular weight hydrophilic materials, to polymeric NMs.[14,17] Firstly, we modified a supported polypyrrole (PPy) matrix by immobilizing Omp2a onto the surface of heterocyclic conducting polymer.[14] The resulting bio-interface, which was hydrophilic, electroactive and biocompatible, promoted the passive transport of ions. More recently, we fabricated bioinspired free-standing NMs (FsNMs) for selective ion transport by

immobilizing the Omp2a β-barrel protein inside nanoperforations created in flexible poly(lactic acid) (PLA) NMs.[17] This functionalization of the nanoperforations caused effects similar to those observed in biological NMs. Moreover, the diffusion of Ca2+ and Na+ ions through Omp2a was found to be significantly higher than for K+, which was attributed to the preference imposed by the protein pore walls. Note that the pores of porins are too large to ensure selectivity, but pores walls are supposed to impart some preferences for ion permeability.[18]

After successful studies on Omp2a-based PPy and PLA biomimetic NMs, in this work we focused on the study of this protein in a more native ambient, similar to that encountered in nature. Amazingly, until now no effort has been made to study Omp2a in a supported lipid bilayer (SLB), which consists in a planar in vitro assembly of lipids sitting on a solid support. In such configuration, which is closer to the natural system than polymeric biomimetic NMs, the structure and properties of the protein have been probed using a variety of surface sensitive atomic force microscopy and electrochemical techniques. More specifically, mechanical mapping with PeakForce Quantitative Nanomechanical Mapping® (QNM) mode, which combines single molecule force spectroscopy with single molecule imaging, has provided information about molecular forces. Furthermore, the function of Omp2a in the SLB has been examined using electrochemical impedance spectroscopy (EIS), and the results have been compared with previous data obtained for Omp2a-based polymeric artificial membranes.

RESULTS AND DISCUSSION

Lipid formulations

The total lipid composition in Brucella melitensis is about 37% of phosphatidylcholine (POPC), 33% of phosphatidylethanolamine (POPE), 20% of

cardiolipine (CL) and 10% of phosphatidylglycerol (POPG).[19] Though POPE is the main phospholipid in many Gram-negative OMs, POPC is the most present in the OM of Brucella melitensis. This particular feature gives to this strain of bacteria high stability in the OM in comparison with other Gram-negative bacteria, whereas the content of POPE in animal cell total lipid membranes is low. For example in the blood cells, POPE and POPG constitute about 6% and 2%, respectively, of all the membrane phospholipids.[20] Indeed, POPC is the major lipid component of the animal cell membranes.[20]

Three different lipid compositions, which consisted on mixtures of POPC, POPE, POPG and/or CL (Scheme 1), were investigated by AFM, TEM, DLS and Z-potential: Mixt-1 composed by 4:3 POPC:POPE; Mixt-2 by 4:3:1 POPC:POPE:POPG; and Mixt-3 by 4:3:1:2 POPC:POPE:POPG:CL.
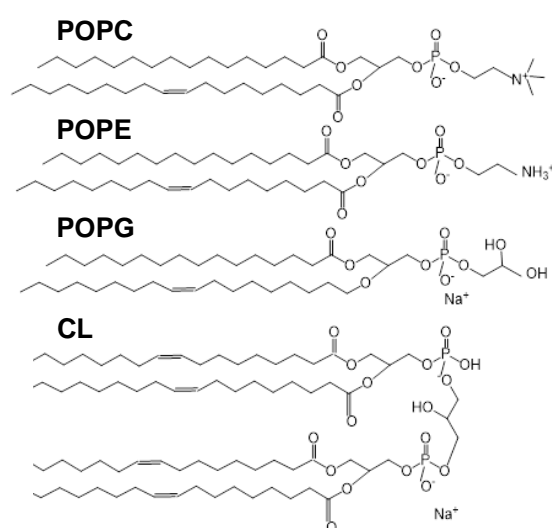
Scheme 1: Chemical composition of the lipids used in this work.

Mixt-1 showed a clear phase separation of the two lipid domains constituted by PE and PC. Specifically, AFM images show that difference in height of the phases is~0.8 nm (Figure 1a) (the bilayer thickness reported for POPC and POPE is 4.33 and 4.03 nm,

respectively[21]). Instead, Mixt-2 displayed the most homogenous and flattest surface, these characteristics being expected to facilitate the rapid recognition of the protein. Consequently, Mixt-2 was selected for further studies with the porin. In this case, the thickness of the bilayer was 5.4 nm, which is significantly lower than the protein's height (around 7 nm) (Figure 1b). Finally, Mixt-3 showed less phase separation than Mixt-1 but still the difference between the domains was also clear, with 1.3 nm height differences (Figure 1c). Furthermore, as the AFM tip was prone to go through the lipid membrane, consequently disrupting the acquiring image, very low forces were needed to achieve its visualization. This feature indicates that the consistency of the lipid bilayer is lower for Mixt-3 than for Mixt-1 and Mixt-2, suggesting that CL increases the fluidity of the lipid bilayer. This hypothesis is supported by the results reported by Unsay *et al.*[22], who found that the fluidity of lipid bilayers increases and its mechanical stability decreases by enhancing the CL concentration. Thus, CL apparently decreases the packing of the lipid membrane.

It should be mentioned that results derived from microscopy techniques can be limited by the drying of the samples, which affects to both AFM and TEM, and/or the deposition of the carbon layer used to support the sample in TEM analyses, which may alters the scattering of electrons. Thus, although the dry-state is by far the most frequent technique for AFM and TEM observations (*i.e.* accompanied with staining for the latter), the drying of the samples on the substrate may cause deformation, or even complete destruction of the sample. However, it has been observed that many block copolymer based assemblies and synthetic lipid bilayers tend to be rigid and, therefore, retain their shape.[23-25] TEM images displayed in Figure 1 show some small irregularities in the edges, suggesting that sizes may be slightly affected by the drying process.

Therefore, dimensions derived from AFM and TEM should be considered as approximate values only.

Dynamic light scattering (DLS) measurements proved that the three mixtures led to several liposome sizes (Figure 1d), with diameters $\phi \approx$ 1075, 555 and 213 nm for Mixt-1, Mixt-2 and Mixt-3, respectively. Besides, the polydispersity in ϕ varied from sample to sample: 0.38, 0.35 and 0.19 for Mixt-1, Mixt-2 and Mixt-3, respectively. On the other hand, the Zeta-potential (ξ) reported for pure POPC, POPE, and POPG phospholipids is -2.3 ± 2.0, -32.4 ± 3.4, and -56.0 ± 2.2 mV, respectively.[26] Interestingly, although POPC and POPE are structurally very similar zwitterionic phospholipids, they were found to exhibit dramatic differences in terms of accessible surface charge.[26] The ξ values determined in neutral water for Mixt-1, Mixt-2 and Mixt-3 were -30±9, -60±9 and -61±8 mV, respectively (Figure 1e). Although POPC and POPE lipids are zwitterions (Scheme 1), Mixt-1 was found to exhibit a moderate negative surface charge at neutral pH. The incorporation of POPG and CL, which contain anionic polar heads (Scheme 1), markedly increased the negative-ξ of the liposomes. This behaviour has been attributed to the fact that negatively charged phosphate group is not counter-posed by any other positively charged group, as occurs in the other two tested lipids (i.e. POPC and POPE).[27]

Figure S1 shows topographic AFM images of SLB obtained from 4:3:1 POPC:POPE:POPG liposomes incubated over mica overnight and diluted in 1× PBS at 1/5, 1/10 and 1/20 ratios. The highest area covered by the lipid bilayer corresponds to the 1/5 dilution, which was selected for further experiments. The breakthrough force of the lipid bilayer was ~0.18 nN and the apparent height 3.4 nm (Figure S2). Clearly, the latter value is underestimated compared with equilibrium thickness of the film. This is related to the fact that in force spectroscopy experiment AFM tip is pushed against the

sample surface leading to elastic deformation of the bilayer before breakthrough event. Hence the measured thickness corresponds to elastically deformed bilayer.

Insertion of Omp2a into lipid bilayers

The protein was inserted into the lipid bilayer by employing two different methods: a) creation of proteoliposomes from detergent-mediated reconstitution of the protein into the preformed liposomes; and b) reconstitution directly incorporating the Omp2a protein into SLBs. The first methodology consists on the following four steps (Figure 2a): (1) Liposomes are detergent-destabilized by titration with Triton X-100, a non-ionic surfactant; (2) Destabilized liposomes are mixed with the detergent-solubilized Omp2a; (3) Detergent is removed with polystyrene beads (Bio-Beads), resulting in the formation of sealed proteoliposomes; and (4) SLB are formed by promoting the fusion of proteoliposomes onto hydrophilic mica substrate. The second approach only needed three steps (Figure 2b): (1) Spreading of liposomes onto mica substrate; (2) Addition of Triton X-100 to destabilize the lipid bilayer; and (3) Protein insertion onto the membrane. Results obtained from each of such two approaches are described below.

Proteoliposomes from detergent-mediated reconstitution of the protein into liposomes

In order to grasp the effect of protein reconstitution onto liposomes, the first mentioned method was studied at 40, 80 and 100 w/w lipid-to-protein ratios using earlier reported protocols.[28-31] In general the diameter of the liposomes was slightly affected by protein reconstitution (Figure 3a), whereas ξ decreased progressively upon the incorporation of either protein or protein buffer into the liposome solution (Figure 3b). On the other hand, comparison of the CD spectra recorded for solutions with the

8

free protein and the different lipid-to-proteins suggest that the protein structure undergoes some changes inside the lipid membrane (Figure 3c). However, in all cases the spectra contained the minimum and maximum ellipticity near 220 and ~195 nm, respectively, indicating that the β-strand rich motives are maintained within the proteoliposomes.[32] Incubation of Omp2a with anionic unilamellar vesicles resulted in the co-sedimentation of a major portion of protein with liposomes after centrifugation, even though some protein was lost during the proteoliposomes purification step, as shown by sodium dodecyl sulphate polyacrylamide gel electrophoresis (SDS-PAGE; Figure 3d). The ratio of protein in the pellet/supernatant was 3, 8 and 4.4 for samples coming from 100, 80 and 40 w/w lipid-to-protein ratios, respectively. Accordingly, the 80 w/w lipid-to-protein proportion allowed the most efficient protein retention. Interestingly, the presence of trimers and dimers is higher in proteoliposomes than in solution. Just 2% of the population presented a trimer organization in the Omp2a free solution (band at 110 KDa in Figure 3d), while increasing to 3.4%, 5.8% and 6.2 % in samples coming from 100, 80 and 40 w/w lipid-to-protein ratio. This feature suggests that protein confinement into lipidic membranes enhances their reorganization, bringing them to a state closer to the natural one.

TEM images of blank liposomes (control) and proteoliposomes (Figures 3e and 3f, respectively) were obtained following the protocol reported by Opalińsky et al.[33] Micrographs denoted that the samples had some polydispersity, the diameters of liposomes and proteoliposomes varying between 100 and 350 nm (Figure 3e) and between 50 and 400 nm (Figure 3f), respectively. The addition of Omp2a to anionic vesicles had some influence on their size and, presumably, shape, which is in full agreement with the results derived from DLS. Proteoliposomes are clearly bigger than control liposomes. In addition, the formers exhibit folds, which may be attributed to the

re-organization induced by the protein reconstitution inside the lipid bilayer (*i.e.* sterically-driven re-organization). However, it should be mentioned that such folds could be also due to an artifact induced by the dry-state. Thus, the above mentioned re-organization could result in a weakening of the interactions inside the lipid bilayer and, consequently, cause deformation upon drying of the sample for TEM observation. On the other hand, the integrity of the membranes was found to be intact after conducting the four steps for protein insertion (Figure 2a).

SLBs were obtained by spreading the control liposomes and the proteoliposomes onto mica substrate. Although the most common procedure to obtain SLBs is the Langmuir-Blodgett method, this technique usually becomes far complicated when multicomponent membranes, like those including OMPs, are studied. Instead, vesicle fusion onto a planar hydrophilic solid support is perfectly suitable for such cases. Different theories have been developed to elucidate how these vesicles spread over the hydrophilic surface. One of the most accepted models assumes that the vesicles adsorb on hydrophilic surface, then undergo substrate-induced deformation which causes their rupture on a solid surface.[34,35] However, the rupture events can be driven by several other factors including fusion between neighbouring vesicles, the high surface density of vesicles, and the presence of active edges of already formed bilayer patches. In this work the SLB formation was performed in the presence of Ca^{2+}, which favours vesicle adsorption onto mica support, especially for those containing negatively charged lipids.[36]

Figure 4 displays AFM images of SLB onto mica substrate obtained after spreading the control liposomes and the proteoliposomes. AFM images acquired for the liposomes reflect a homogenous and flat surface (Figure 4a), with an average roughness of (0.15 ± 0.01 nm). Representative cross-sectional profiles indicate that the treatment for

obtaining proteoliposomes does not cause protrusions in the lipid bilayer. Instead, small protuberances of ~2 nm in height and ~25 nm in width appear upon the incorporation of Omp2a (Figures 4b-d). Moreover, AFM images evidence that the amount of protuberances decreases with increasing lipid-to-protein ratio, while the size of the protuberances increases. More specifically, the amount of protuberances decreases ~25% and ~35% when the from the lipid-to-protein ratio increases from 40 w/w to 80 and 100 w/w, respectively. It is worth noting that large aggregates (~4 nm in height and ~100 nm in width) appeared for the highest concentration of protein (Figure 4c), limiting protein nanomechanical studies.

Magnified AFM images provide improved visualization of the protein's shape (Figures 4b-d). More specifically, magnification of the SLB derived from proteoliposomes obtained using 80 w/w lipid-to-protein ratio reflects structures of 1.5-2 nm in height and 10 nm in width, with small cavities in the middle. This condition seems to be the ideal in terms of protein's reconstitution efficiency and visualization. Therefore, more insights of this condition are shown in Figure 5a, where AFM images of different patches on this surface are displayed. Comparison with the TEM images of the free protein in solution, which are shown in Figure 5b, suggests that such small patches on the membrane correspond to clusters of 5 to 10 monomers laterally associated. A membrane surface screening allowed to separate large protein-detergent aggregates (> 50 nm, dark blue in Figure 5c) from small clusters of proteins (<50 nm, light blue in Figure 5c). Analysis of the height for the population of small clusters indicates an average value of 2.3 ± 0.5 nm (Figure 5d), which is in accordance with the protein and lipids heights.[37]

Omp2a reconstitution by direct incorporation into the SLB

The alternative method of incorporation of Omp2a into SLBs, which is schematized in Figure 2b, was followed using AFM analysis at high resolution. The main assumption for this approach was deeply investigated by Milhiet *et al.*,[38] and is based on the insertion of proteins into the destabilized SLB after its deposition onto the mica substrate. In a very recent work Sumino *et al.*[39] directly attached transmembrane proteins, which were solubilized with an histidine-tag, to a Ni^{2+} coated mica surface. After this, detergent destabilized liposomes were added in order to fill the space between the proteins, achieving an oriented reconstitution.

In this work, SLBs were disrupted by the addition of Triton-X 100 and, afterwards, the protein was incorporated. Figure 6 displays topographic AFM images of SLB obtained from POPC:POPE:POPG (4:3:1) liposomes at the three different steps of the reconstitution process. The spread liposomes, where two faces can be visualized, are shown in Figure 6a. After incubation with 0.01% Triton X-100 to destabilize the membrane, noticeable changes were observed (Figure 6b), that is, the surface became flatter and more homogeneous. Finally, the bilayer was further incubated in a protein refolding solution with 10 µg/mL of Omp2a. At this point, large protrusions from the lipid bilayer emerged (Figure 6c). The width and height of such protrusions were 93 and 2.3 nm, as is evidenced by vertical profiles extracted from the AFM images (red lines in Figure 6c). Nevertheless, no single units of protein were detected. Instead the bilayer was broken in many sites and agglomerates of protein were found. This was attributed to the fact that the concentration of Omp2a used in this process was too high. In addition, previous studies suggested that lipid bilayers could be destabilized by the detergent used in the refolding solution.[40]

In order to overcome the limitation associated to the protein concentration, the latter was reduced. As occurred above, the surface of spread liposomes (Figure 7a) became

flatter and more homogeneous after incubation with 0.01% Triton X-100 (Figure 7b). After incubation in a 2 µg/mL Omp2a refolding solution, some breakages and agglomerates were also visualized (Figure 7c), even though at such low concentration single protein's shape could be identified when higher contrasts were used. The recognized protein was around 10 nm wide and 1.5 nm height, showing a deeper part in the middle, as it was expected.

In summary, although high resolution images of the proteins reconstituted into the lipid bilayer were obtained, this strategy is limited by the adverse effects caused by the detergent used for the refolding. Thus, the lipid bilayer is still disrupted when the protein concentration is reduced from 10 to 2 µg/mL. Due to this drawback, the strategy based on detergent-mediated reconstitution of the protein into liposomes (Figure 2a) was used to insert the Omp2a into the lipid bilayer for both nanomechanical and functional studies. Specifically, this methodology allows a higher control of the process, as is proved by the fact that the substrate surface is homogeneously coated by the lipid bilayer and a homogeneous protein distribution into the bilayer is observed.

Nanomechanical properties of Omp2-containing SLBs prepared using preformed liposomes

Lateral organization of lipid, carbohydrates and proteins found in biological membranes is involved in many cellular events, for example signal transduction or membrane fusion.[41] Furthermore, structural, physical and chemical properties of biomacromolecules can control their activity at different length-scales. In particular, nanomechanical properties can affect some biological functions of proteins in processes such as cell signalling, membrane signal transduction and immune responses.[42-44] For example, antibodies need high flexibility to bind to diversified antigens.[44] Accordingly,

deep-end studies on how proteins modify the consistency of lipid bilayers and how soft proteins are in comparison with the hosting lipid bilayers are not only attractive but also very relevant from a biotechnological point of view. Due to recent advances in AFM technologies, it is currently possible to measure mechanical properties of single molecules in physiological conditions. Thus, force-distance (FD) curves, which are directly obtained from cantilever's deflection, can be collected at the same time as the AFM images are acquired. For each pixel of the topographic image, the AFM records FD curves with Ångstrom precision and piconewton sensitivity. More specifically, interaction forces between the AFM stylus and the biological sample surface are mapped pixel-by-pixel, enabling quantification of the elastic modulus, adhesion forces and deformation of the sample simultaneously.[45] In this work, the elasticity has been extracted using the Derjaguin-Muller-Toporov (DMT) model,[46] whereas the adhesion force has been acquired from the vertical difference of the minimum force during retraction and the zero-force. Lipid bilayers were examined using a soft cantilever (nominal spring constant k_s= 0.7 N/m) with the set point adjusted to get minimum sample deformation.

Figure 8a shows a 2×2 µm^2 topographic image of Omp2a molecules embedded on the lipid membrane over a mica substrate, which was obtained in the peak force QNM tapping mode. The peak force set point was adjusted to a force of 544 pN. For analysis, a cross-sectional profile of 2 µm length (dashed red line) is plotted next to the AFM windows. The DMT modulus map (Figure 8b) reflects the presence of two domains with different constant elasticities, corresponding to the lipid bilayer surface and to the Omp2a molecules. Figure 8b includes the profile of elasticity fitted with the DMT modulus. The mean DMT modulus obtained for the lipid bilayer and Omp2a are 19 MPa and 10.5 ± 1.7 MPa, respectively, the latter being obtained by selecting aggregates

smaller than 40 nm. These results are consistent with high resolution topographic AFM studies on OmpG reconstituted into native *E. coli* lipids that evidenced that the OMP is softer than the lipid bilayer,[45,47] even though no quantitative estimation of the elastic modulus was provided. However, studies on other related proteins (*i.e.* bacteriorhodopsin and multiprotein complexes contained in erythrocyte membrane) using quantitative mechanical AFM mapping[48,49] and micro-second force spectroscopy[50] probed that the stiffness of MPs depends on the environment (*e.g.* electrolyte identity and concentration, pH and substrate), ranging from a few MPa to tens of MPa. Similarly, the reported moduli of lipid bilayers ranged from ~10 to ~500 MPa depending on the chemical identity and environment.[51,52] However, the modulus of elasticity of ~18 MPa was recently reported for L_α phase of mica-supported bilayer composed of lipids extracted from *E. coli*.[53] Moreover, the modulus of polymeric FsNMs was reported to increase from ~25 to ~35 MPa with the thickness (*i.e.* from 10-20 nm to ~80 nm).[54]

Figure 8c displays, in one hand, the adhesion map, as obtained from the FD curves recorded in each pixel, and, in the other hand, both the profile and histogram of the difference between lipid bilayer and protein adhesion. It should be noted that the DMT model used in this work is appropriated for weak adhesive forces and tips with a small curvature radius.[55] The adhesion force of the SLB was around 200 pN, while that of Omp2a was 161.9 ± 9 pN. Lipids therefore adhered more to the AFM tip than the protein, which should be attributed to the asymmetric distributions of van der Waals forces. Consequently, the tip forms stronger interactions with the flat surface of lipids than with the curved surface of Omp2a, the latter providing less contact area.[56] It is worth noting that the adhesion forces determined for the lipid bilayer and the OMP are one order of magnitude smaller than those reported for polymeric FsNMs.[17] More

specifically, the adhesion force of polymeric FsNMs were found to be comprised between 5 and 7 nN.[54]

Two phases are also observed in the representative deformation map displayed in Figure 8d. Indeed, the corresponding profile and histogram provided deformation values of ~1 nm and 4.6 ± 0.7 nm for the SLB and Omp2a, respectively. These results prove that mechanical properties such as the elasticity or deformation can be imaged at high resolution. Strikingly, the contour of single molecules becomes apparent when their mechanical properties are studied, even though their recognition becomes easier when height images are also considered. Similar analyses were performed for the control SLBs (*i.e.* liposomes treated like the proteoliposomes) onto mica substrate (Figure S3). Results corroborated that nanofeatures previously described were due to the protein reconstitution. Thus, no small protrusion was observed in Figure S3 and, in addition, no significant changes in the DMT modulus, adhesion and deformation were detected when comparing values obtained for SLBs with and without protein.

Overall, comparison of the results obtained in this section with those reported for polymeric NMs[54] indicates that immobilization of OMPs inside the nanopores of polymer-based FsNMs offers advantages over the lipid bilayer-based approaches. Indeed, although synthetic lipid bilayers, like those studied in this work, are more stable than pure biological membranes, their mechanical strength is lower than that of polymeric NMs. The fragility of lipid bilayers may be a handicap for practical applications, while the mechanical flexibility and resistance of polymeric FsNM were reported to be enough for this purpose. Thus, in many practical applications, as for example those related with molecular filtration, nanofluidics and nanodetection, stable FsNMs are needed to sustain mechanical stress during the fabrication and operation processes.

Electrochemical detection of Omp2a in proteoliposomes

Electrochemical methods are widely accepted to detect residues with redox properties in proteins, such as tyrosine (Tyr) and tryptophan (Trp).[57,58] Among the different electrochemical strategies (*e.g.* sweep voltammetry and cyclic voltammetry), square-wave voltammetry (SWV) stands out since high peak resolution is obtained with very low peptide and protein concentrations after correcting with an efficient base line.[59] In addition, the usage of electrochemical method has the advantage that proteins can be easily adsorbed on many surfaces facilitating the preparation of protein-modified electrodes.[60]

It is well-known that the peak potential of Tyr and Trp depend on the buffer. Thus, Vacek *et al.*[61] showed that pH plays a key role on the peak potential, which shifts towards less positive values with increasing pH. Furthermore, analysis of the peak potential shifts at a given buffer conditions allows to discriminate between native and denatured forms of proteins.[57] Omp2a contains 22 Tyr and 10 Trp residues which are mainly located in the external part of the barrel in the native protein. Therefore, in proteoliposomes are expected to be at the interface between the lipid bilayer and the medium if the protein remains stable. In order to prove the stability of the protein native form in the proteoliposomes, characterization of the Omp2a Tyr and Trp residues has been performed by applying the label-free and sensitive SWV methodology. Specifically, the response of the protein when it is alone (control of the native form) and embedded into the lipid bilayer has been compared.

Three negative controls were analysed: bare glassy carbon electrode (GCE), GCE covered by 2-methyl-2,4-pentanediol-containing refolding buffer (GCE+MPD), and GCE covered by the spread liposomes (GCE+liposomes). As it can be seen in Figure 9,

none of the mentioned samples gave rise to any substantial peak. Instead, when the protein was adsorbed with the refolding buffer two peaks can be visualized. These correspond to the oxidation peaks of Tyr and Trp (+0.45 V and +0.62 V, respectively). The peak current density is much higher for the first than for second, which is fully consistent with the larger quantity of Tyr than Trp in the Omp2a sequence. In contrast, a single less intense peak at +0.5 V was found when proteoliposomes were spread onto the glassy carbon surface. This is correlated with the lower protein presence on the proteoliposomes since there is not a complete protein loading and, therefore, the monitoring of the Trp signal becomes more difficult.

Functionality of Omp2a in SLBs

The chemical environment is critical to maintain the biological functionality of OMPs. Hence, biological nanopores offer precise control over ion selectivity rectification and gating as well as outstanding permeability. Molecular recognition is the hallmark of biological interactions to enable these functions, especially the ion selectivity, so that embedded biochannels often lose their activity upon leaving the biological environment. Several strategies have been studied to transfer properties of naturally occurring nanopores to supported polymeric NMs. For example, incorporation of lipid bilayer onto supported NM[10,62-64] and functionalization of the nanopores surfaces through ligands[65-68] are considered as the most reliable ones. Nevertheless, the utilization of supported NMs drastically limits the practical application of the device and, unfortunately, functionalization of nanopores surfaces in polymeric FsNMs is not an easy task. In order to engineer new strategies for the fabrication of more effective bioinspired FsNMs, we devoted this section to study the functionality of Omp2a-

immobilized inside SLB, and its comparison to the results reported for Omp2a-based PLA FsNMs.[17]

The electrochemical impedance (EIS) method has been employed to measure the current through electrodes covered by the systems investigated in this study. This technique exploits the fact that lipid bilayers are electrically resistant and behave as insulators, monitoring the membrane conductance related to the transport of ions. In this work, the electrode used for the functional characterization is indium tin oxide (ITO) supported on glass, which is a suitable substrate for the characterization of lipid bilayer membranes and does not induce protein denaturation.[69-72] The complex EIS signal has been related to the electrical properties of each component of the system (*i.e.* the electrode, the lipid bilayer with or without protein, and the electrolyte, KCl), representing them as electrical elements on an electric equivalent circuit (EEC). Each element contributes at different frequency regime enabling the separation of the effects of the components at the interface. The quality of the fitting between the experimental data and the ECC has been proved by the evaluating the percentage error associated to each circuit element, which is lower than 10% in all cases.

Consistently with our previous work on Omp2a-filled nanoperforated PLA FsNMs, the EEC (Figure 10a) obtained for bare ITO electrodes shows the electrolyte resistance (R_S) connected in series with the constant phase element (CPE) of the double layer semiconductor/electrolyte interface, (Q_{dl}).[17] Here, lipid bilayer-coated electrodes behave as a circuit in which the R_S is followed by the lipid membrane CPE element (Q_M) in parallel with the membrane resistance (R_M) and the semiconductor/electrolyte interface Q_{dl} element, which arises from lipid bilayer defects (*i.e.* lipid bilayers are dynamic in nature and, therefore, the apparition of changing defects and holes is expected to be

relatively frequent). Moreover, this EEC is not altered by the incorporation of Omp2a inside the bilayer (Figure 10a).

Figure 10b displays the Nyquist plots recorded for the bare ITO substrate and four different lipid bilayers (*i.e.* lipid bilayers using 40, 80 and 100 w/w lipid-to-protein ratio and lipid bilayer without protein) using 0.1 M KCl aqueous solution. All four bilayers display curves with one semicircle in the high frequency range, and a straight ascending line in the low frequency range. The starting point of the curve indicates R_S, while the diameter of the semicircle corresponds to the charge-transfer resistance, R_M. Besides, the conductivity calculated for each system is represented in Figure 10c. The membrane conductivity (σ, in S/cm) has been determined using the following expression:

$$\sigma = \frac{L}{R_M A} \qquad (3)$$

where L is the thickness of the membrane (5.5×10^{-7} cm), A is the area of the electrode (0.5 cm^2), and R_M is the membrane resistance. As expected, the membrane conductivity increases as a function of the protein concentration on the lipid bilayer, being significantly higher for the 40 w/w lipid-to-protein ratio.

Figure 10d displays the Bode plots obtained for each condition, where both the difference of logarithmic impedance *vs* the logarithm of frequency (log f, where f is expressed in Hz) and the change in phase angle *vs* the logarithm of frequency are represented. Bare ITO shows a steady increase of the impedance signal log f below 3, the same being observed in the difference of phase angle. Instead, when the electrode was covered by the lipid bilayer (with/without protein) a well-defined shoulder appeared at the log f regime of 1-3. This is related to the resistance and constant phase element (Q_M) induced by the presence of the lipid bilayer.

The resistance obtained for the lipid bilayer alone (4.2 K$\Omega \cdot$cm^2) (Table 1), which is close to that reported for single component 1,2-dimyristoyl-sn-glycero-3-phosphocholine bilayer,[73] is significantly lower than that previously reported for non-perforated PLA FsNMs (7.4 K$\Omega \cdot$cm^2)[17] but higher than what was obtained for supported PPy membranes (821 $\Omega \cdot$cm^2).[14] According to these results, ion diffusion decreases as follows: supported PPy >> SLB > PLA. This relative order can be explained considering, on the one hand, that the average thickness of insulating PLA NMs (~100 nm) is very high compared to the one of lipid bilayers (~5 nm) and, on the other hand, that PPy is a conducting polymer, which facilitates the electron transfer to the electrode surface. Furthermore, the resistance of 40 w/w lipid-to-protein ratio SLBs (1.5 K$\Omega \cdot$cm^2) is relatively similar to that of nanoperforated Omp2a-filled PLA FsNMs (1.9 K$\Omega \cdot$cm^2)[17] and higher than that of PPy-Omp2a (243 $\Omega \cdot$cm^2).[14] As expected, the reduction in the resistance of each Omp2a-containing system with respect to its corresponding non-functionalized analog evidences that the incorporation of the porin channel enhances ion diffusion in all cases. Moreover, the affinity of K$^+$ ions towards the protein-containing systems follows this order: PPy >> SLB $\approx$ PLA.

The resistance values obtained in this work for lipid bilayers are smaller than those previously reported in literature (*i.e.* > 80 K$\Omega \cdot$cm^2).[2] This observation could be attributed to one of the following two reasons or to the combination of both. First, the ion concentration used in this work (*i.e.* 0.1 M KCl), which was chosen for consistency with our previous studies on Omp2a-based PPy and PLA bioinspired NMs,[14,17] is one order of magnitude higher than the one typically used. It is worth noting that when higher is the electrolyte concentration, lower is the membrane resistance.[3] Also, the presence of defects in the bilayer and the consequent reduction in the packing density of the immobilized lipids can explain the low resistances determined in this work, in

comparison with those obtained in other studies.[2] Thus, such imperfections could be due to the difficulty of completely covering the ITO surface with the lipid bilayer.

CONCLUSIONS

The nanomechanical properties and functionality of Omp2a reconstituted into SLBs have been evaluated and compared with those of bioinspired Omp2a-polymeric NMs. Among the three tested lipid compositions, bilayers made of 4:3:1 POPC:POPE:POPG have been found to be the most homogenous and consistent. Besides, reconstitution of the OMP into preformed liposomes using detergent as mediator has allowed obtaining homogenous and reproducible surfaces. The estimated average DMT moduli, adhesion force and deformation of Omp2a is 10.5±1.7 MPa, 161.9±9 pN and 4.6 0.7 nm, respectively. These values are clearly distinguishable from the ones determined for the lipid bilayer, reflecting the satisfactory incorporation of the OMP. The low stiffness of Omp2a and its high deformability compared with the dimensions of the molecule (nominal height: 7 nm) reflect a high molecular flexibility. This key property, which is related to the conformational adaptability of the protein, could be responsible of an essential aspect of Omp2a biological functionality: it allows the passage of a number of molecules with varying sizes and shapes to ensure the nutrition of the bacteria. On the other hand, the ion affinity significantly increases with the protein concentration used in the proteoliposomes reconstitution, a reduction of ~78% being observed between the control and the lowest lipid-to-protein ratio.

In summary, the reconstitution of OMPs into lipid bilayers provides platforms that fulfil both the nanometric dimensional requisite for truly mimicking biological attributes, and the conditions necessary for exploring their properties. In spite of these advantages, the properties Omp2a-based SLBs are less suitable for technological

applications than those of polymeric FsNMs with Omp2a immobilized in nanoperforations. Our future research in this field will focus on the integration of such two platforms to collect in a single system their potential individual benefits. Thus, we plan to immobilize Omp2a-based lipid bilayers into the pores of nanoperforated polymeric membranes to improve the ion affinity detection capability. This system is expected to be the most versatile from a biotechnological point of view since the protein environment will be very close to native conditions and, therefore, the negative influence of the polymer in the protein structure will be eliminated.

METHODS

Expression, purification and refolding of the Omp2a outer membrane protein from _Brucella melitensis_

Bacterial strain and growth. Cells of _E. coli_ BL21 (DE3) carrying pLysS and pET2a plasmids (containing the gene Omp2a without peptide signal) were grown in LB medium at 37°C with constant shaking. Log cultures (OD 0.6) of 500 mL were stimulated with IPTG (0.2 mg mL-1) for 3 h. Cells were then harvested by centrifugation at 4,000 g for 30 min, the resulting bacterial pellets being stored at -20°C.

Overexpression and non-native purification of Omp2a. The bacterial pellets were thawed and treated with 8 mL of TEN lysis buffer (50 mM Tris–HCl pH 8, 1 mM EDTA, 17 mM NaCl, 125 mM PMSF, 250 mg mL-1 lysozyme) for 20 min at 25°C. Harvested cells were further broken by addition of 10 mg of sodium deoxycholate for 60 min at 37°C with constant shaking, and 2 mg of DNase I for 60 min at 25°C. The suspension was then centrifuged at 14,000 g for 20 min at 4°C. The resulting pellet underwent a washing buffer (2 M urea, 20 mM Tris–HCl pH 8, 500 mM NaCl, 2% Triton X-100) and centrifuged at 14,000 g for 20 min at 4°C. The inclusion bodies were

solubilized with 8 mL of TEN buffer (50 mM Tris–HCl pH 8, 1 mM EDTA, 17 mM NaCl, 8 M urea). Then, the solubilized proteins were applied onto an anion-exchange DEAE column previously equilibrated with 25 mL of buffer (50 mM Tris–HCl pH 8, 17 mM NaCl, 8 M urea). Omp2a was eluted with a 50 mL linear gradient of NaCl from 17 to 500 mM, whereas the protein profile was further analyzed using SDS–PAGE. Fractions containing 39 kDa proteins were then pooled and stored at 4°C.

Omp2a refolding in sodium dodecyl sulfate – 2-Methyl-2,4-pentanediol (SDS – MPD) system. To refold Omp2a, the protein solution (1 mg/mL protein, 250 mM NaCl, 50 mM Tris–HCl pH 8, and 8 M urea) was eluted onto a PD-10 column to exchange the buffer (150 mM NaCl, 50 mM Tris–HCl pH 8, and 120 mM SDS, which is 15 times the critical micellar concentration). SDS-unfolded samples were then diluted 1:1 in a refolding solution (50 mM Tris–HCl pH 8, 150 mM NaCl, 3 M MPD). The protein solution was then incubated at room temperature. The samples were stored at −20°C to stop the refolding reaction. Hereafter, Omp2a protein at this procedure stage is named as obtained Omp2a.

Liposomes production

The procedure used to produce liposomes is depicted in Scheme 2. Initially, liposomes were generated by dissolving and mixing lipids in 4:1 chloroform:methanol, which assured an homogeneous mixture (1). After this, the solvent was evaporated using argon stream and agitation to yield a thin lipid film (2). The film was thoroughly dried to remove residual organic solvent by placing the vial on a vacuum pump for 30 min. Then, film-rehydration was performed by adding the adequate buffer (3) and sonicated 30 min at 37º (4). Vesicles were stored at 4º C. Liposome solutions were diluted 1/5 and deposited over the mica substrate for analyses with the AFM (5).
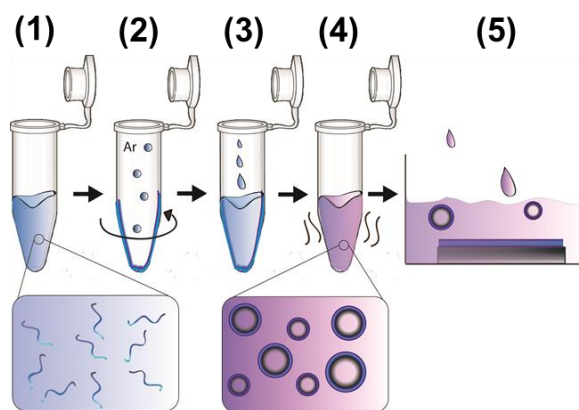
Scheme 2: Fabrication of liposomes

Formation of proteoliposomes from preformed liposomes

Shortly, liposomes were detergent-destabilized by titration with Triton X-100 and, subsequently, mixed with the detergent-solubilized Omp2a transmembrane protein. After this, controlled removal of the detergent by polystyrene beads (Bio-Beads) resulted in the formation of sealed proteoliposomes. Then, the proteoliposomes were incubated onto the mica substrate in order to facilitate their spreading.

Strategy of protein reconstitution by direct incorporation into SLBs

SLBs were first incubated 15 min at room temperature in the presence of the detergent (Triton X-100 at 0.01%) in order to destabilize the membrane. After this, they were further incubated at the same temperature with detergent-solubilized proteins (10 or 2 μg/mL), allowing them to be inserted into the membrane. The excess of detergent and proteins was removed by extensive washing with mQ water.

SDS-PAGE

Proteoliposomes were pelleted by ultracentrifugation (15 min, 10,000 g) and the pellet was re-suspended in 25 μL of loading buffer. The protein in the supernatant and

pellet (equal volumes) were subsequently subjected to glycine SDS–PAGE using 15% acrylamide gels and visualized with Comassie Blue.

Dynamic light scattering (DLS)

The size distribution of the protein in 1× PBS pH 7.4 and in 50 mM Tris–HCl pH 8, 150 mM NaCl, 3 M MPD was determined using a NanoBrook Omni Zeta Potential Analyzer from Brookheaven Instruments Corporation. Particularly, three consecutive runs of 60 seconds each were conducted for every sample.

AFM measurements

Topography imaging of the samples was performed with 5500AFM (Keysight) operating in MAC mode. In this intermittent contact mode magnetically coated cantilevers are driven by an oscillating magnetic field. This enables elimination of spurious responses generated by cantilever holding mechanism or the surrounding fluid. For imaging, we have used MAC Levers VII with nominal spring constant of 0.14 N/m, but its exact value was determined for each individual tip from thermal tuning. Nanomechanical measurements were carried out with Dimension Icon (Bruker) instrument operating in Peak Force QNM mode, which enables simultaneous imaging of the topography and mapping of the nanomechanical properties of the sample. In this mode, Z-piezo is modulated at the frequency of 2 kHz with default peak force amplitude and during each cycle the force-distance curve is recorded for every pixel of the scanned area. Based on analysis of the retract curves, it is possible to determine the adhesion force (F_{adh}) and reduced modulus of elasticity (E^{*}) according to Derjaguin, Muller, Toporov (DMT) contact mechanics model:

$$F_{tip} = \frac{4}{3}E^*\sqrt{Rd^3} + F_{adh} \qquad (1)$$

where F_{tip} denotes force acting on AFM tip, d defines the distance between said tip and the sample surface and R is the tip radius. Modulus of elasticity (E_s) for given sample can be estimated using equation:

$$E^* = \left[\frac{1-v_t^2}{E_t} + \frac{1-v_s^2}{E_s}\right]^{-1} \qquad (2)$$

where v_t and v_s are Poisson's ratios for the material of the tip and the sample respectively, while E_t denotes modulus of elasticity of the tip material. In order to calibrate the instrument, determination of modulus of elasticity was evaluated using PDMS test sample (Bruker) with nominal value of modulus of elasticity equal 3.5 MPa. All images/maps were acquired in aqueous buffers. We have used Scan Asyst Fluid+ cantilevers (Bruker) with nominal spring constant of 0.7 N/m and the nominal tip radius of 5 nm. However, the exact value of spring constant for each cantilever was obtained from thermal tune method.

Transmission electron microscopy (TEM)

The liposomes and proteoliposomes were placed on carbon-coated grids and stained with 0.5% uranyl acetate and examined by electron microscopy. Solution containing Omp2a (0.34 mg/mL) was dispersed on glow-discharged carbon coated copper grids (300 mesh) and negatively stained with uranyl acetate (2.0 % w/v). After incubation (30 s), the excess of protein was removed with filter paper, and the grids air dried for a further 1-2 s. TEM images were obtained with a Philips TECNAI 10 electron microscope operating at 100 kV.

Circular dichroism (CD)

CD measurements were performed on a Chirascan-plus *q*CD spectrometer (Applied Photophysics, APL; UK) equipped with a temperature-controlled cell, using a call path length 10 mm. Spectra were recorded between 180 and 260 nm. Machine settings were as follows: 1 nm bandwidth, 1 s response, 0.5 nm data pitch, 100 nm/min scan speed and cell length of 0.1 cm. All CD spectra presented in this work correspond to the average from three independent measurements.

Square-wave voltammetry (SWV)

SWV experiments were carried out using glassy carbon electrodes (GCE) (2 mm diameter) as anodes. Before conducting any experiment, the GCE was mechanically polished with powder of alumina to produce a mirror-like surface. The electrodes were subsequently sonicated to remove adhered alumina particles, rinsed with water, and left to dry. Finally, 5 µL of the corresponding sample were deposited on the top of the surface

Electrochemical characterization was carried with an Autolab PGSTAT302N. Experiments were conducted in a phosphate buffer solution (PBS) 0.1 M (pH = 7.4) at room temperature. The initial and final potential were 0 V and + 1 V. SWV amplitude: 25 mV, frequency: 20.

Electrochemical Impedance Spectroscopy (EIS)

EIS measurements were performed using a conventional three-electrode cell and an AUTOLAB-302N potentiostat/galvanostat operating between the frequency range of 104.5 Hz and 10-2 Hz and 5 mV of amplitude for the sinusoidal voltage. All

experiments were performed at room temperature with lipid bilayers deposited onto ITO and using 100 mM KCl. ITO was used as working-electrode and platinum as counter-electrode, whereas Ag|AgCl saturated (KCl 3M) was employed as reference electrode. After data collection, EIS results were processed and fitted to an electrical equivalent circuit (EEC).

SUPPORTING INFORMATION

The Supporting Information is available free of charge on ACS Publication website. Description of the experimental methods. AFM images and force-distance curve-based AFM of SLB obtained from 4:3:1 PC:PE:PG liposomes.

ACKNOWLEDGEMENTS

AUTHOR INFORMATION

Anna Puiggalí-Jou: anna.puiggali@upc.edu

Jan Pawlowski: jpawlowski@chem.uw.edu.pl

Luis J. del Valle: luis.javier.del.valle@upc.edu

Catherine Michaux: catherine.michaux@unamur.be

Eric A. Perpète: eric.perpete@unamur.be

Slawomir Sek: slasek@chem.uw.edu.pl

Carlos Alemán: carlos.aleman@upc.edu

CAPTIONS TO FIGURES

Figure 1. Topographic AFM images with the corresponding vertical profiles and TEM images of SLBs obtained from liposomes composed of: (a) 4:3 POPC:POPE (Mixt-1); (b) 4:3:1 POPC:POPE:POPG (Mixt-2); and (c) 4:3:1:2 POPC:POPE:POPG:CL (Mixt-3) diluted 1/5 in 1× PBS. The red lines in the AFM images (a-c) indicate where from the vertical profile shown next to each image has been extracted. (d) DLS graph expressing the intensity *vs* diameter and (e) the Z-potential (e) of the Mixt-1, Mixt-2 and Mixt3.

Figure 2. The protein was inserted on the lipid bilayer using two different methods: (a) Formation of proteoliposomes from preformed liposomes; and (b) Insertion of the Omp2a protein by direct incorporation the Omp2a protein into SLBs. The four and three-steps of approaches (a) and (b) are described in the text.

Figure 3. DLS results expressed in term of (a) intensity *vs* diameter, (b) ξ values and (c) CD spectra of proteoliposomes prepared from detergent-mediated reconstitution of the protein using 40, 80 and 100 w/w lipid-to-protein ratio, control liposomes (*i.e.* preformed liposomes), blank liposomes (*i.e.* preformed liposomes altered by adding the reconstitution detergent medium but without protein) and Omp2a solution. (d) SDS-PAGE gel for the proteoliposomes. TEM micrographs of (e) blank liposomes and (f) proteoliposomes prepared using 80 w/w lipid-to-protein ratio. Histograms showing the diameter distributions are also displayed.

Figure 4. Topographic AFM images (first row) of SLB obtained from (a) POPC:POPE:POPG (4:3:1) liposomes or from proteoliposomes achieved using (b) 40, (c) 80 and (d) 100 w/w lipid-to-protein ratios spread over mica. Data were recorded on buffer solution (150 mM KCl, 10 mM Tris-HCl, pH 7.8). The red lines in AFM images indicate where from the vertical profile shown below (second row) each image has been

extracted. Also, insets of each AFM image and profile are shown below (third and fourth rows, respectively).

Figure 5. (a) Representative topographic AFM images of SLB obtained from POPC:POPE:POPG (4:3:1) proteoliposomes (80 w/w lipid-to-protein ratio) spread over mica. The red lines in the AFM images indicate the region used to extract vertical profile shown next to each image. (b) TEM images of Omp2a stained with uranyl acetate (scale bar: 10 nm). (c) Representative topographic AFM images of SLB obtained from POPC:POPE:POPG (4:3:1) proteoliposomes (80 w/w lipid-to-protein ratio) spread over mica. Particle analyses were performed on 2×2 μm^2 images. Light blue regions indicate particles below 45 nm (protein oligomers) while dark blue spots correspond to particles above 45 nm (protein aggregates). Data were recorded with a buffer solution (150 mM KCl, 10 mM Tris-HCl, pH 7.8). (d) Particle dimeter distribution and height distribution of protein oligomers (< 45 nm).

Figure 6. Topographic AFM images of: (a) SLB obtained from POPC:POPE:POPG (4:3:1) liposomes, (b) after being incubated with 0.01 %Triton X-100, and (c) further incubated in a refolding solution with 10 µg/mL of Omp2a. Data were recorded on buffer solution (150 mM KCl, 10 mM Tris-HCl, pH 7.8). The red lines in the AFM images (a-c) indicate where from the vertical profiles shown below have been extracted.

Figure 7. Topographic AFM images of: (a) SLB obtained from POPC:POPE:POPG (4:3:1) liposomes, (b) after being incubated with 0.01 %Triton X-100, and (c) further incubated in a refolding solution with 2 µg/mL of Omp2a. Data were recorded with the buffer solution (150 mM KCl, 10 mM Tris-HCl, pH 7.8). The red square shows where the inset has been obtained from. The red line in the AFM image indicates (c) where from the vertical profile shown below has been extracted. Red circles correspond to protein agglomerates.

Figure 8. FD-based AFM images of POPC:POPE:POPG (4:3:1) proteoliposomes (80 w/w lipid-to-protein ratio) spread onto mica: (a) topography, (b) DMT modulus map, (c) adhesion map and (d) deformation map. Data were recorded with the buffer solution (150 mM KCl, 10 mM Tris-HCl, pH 7.8). The red lines in the AFM images (a-d) indicate where from the vertical profile shown below or next to each image has been extracted. The histograms below the profiles express the percentage of particles below 45 nm in diameter (protein oligomers) *vs* the difference in the indicated parameter with respect to lipid bilayer values.

Figure 9. Voltammograms of SWV obtained for bare glassy carbon electrode (CGE) and GCE covered by 2-methyl-2,4-pentanediol-containing refolding buffer (GCE+MPD), spread liposomes (GCE+liposomes) and spread proteoliposomes (GCE+proteoliposomes).

Figure 10. (a) Schemes representing the ITO, the lipid bilayer and the lipid bilayer containing Omp2a with the corresponding EEC used for fitting the experimental data from EIS measurements: R_S is the electrolyte resistance; Q_M and R_M are the membrane constant phase element and resistance, respectively; and Q_{dl} is the double layer constant phase element for the electrode surface. (b) Nyquist plots of ITO (green stars), lipid bilayer (purple triangles), lipid bilayer with the reconstituted protein at 100 (blue circles), 80 (red diamonds) and 40 w/w (black squares) lipid-to-protein ratio in 0.1 M KCl. Symbols correspond to experimental data, while lines are the fitted curves according to EEC. (c) Average conductance measured for the lipid bilayer and those containing the protein at different lipid-to-protein ratios. (d) Bode plots of the systems described in (b).

(a) Mixt-1: 4:3 POPC:POPE
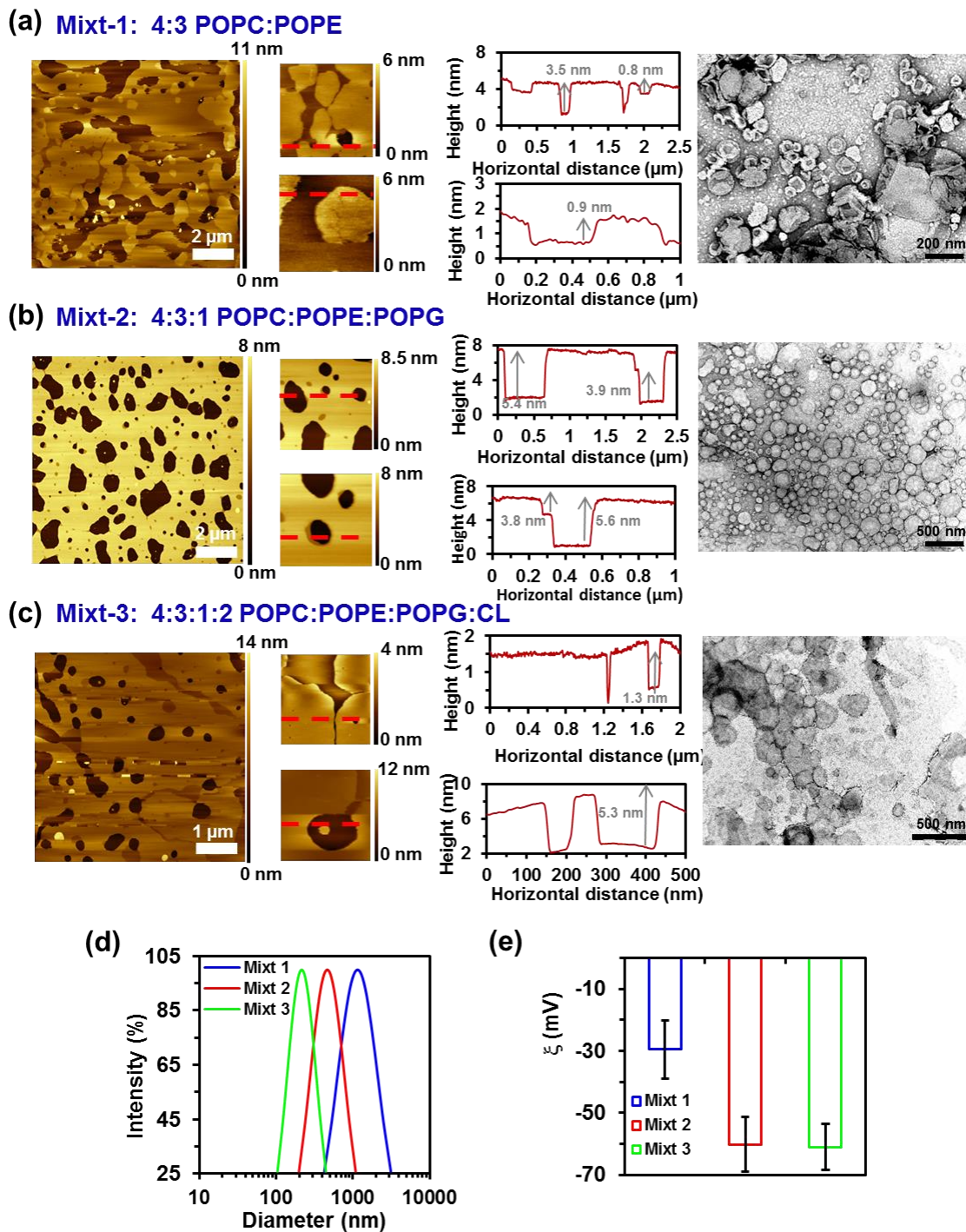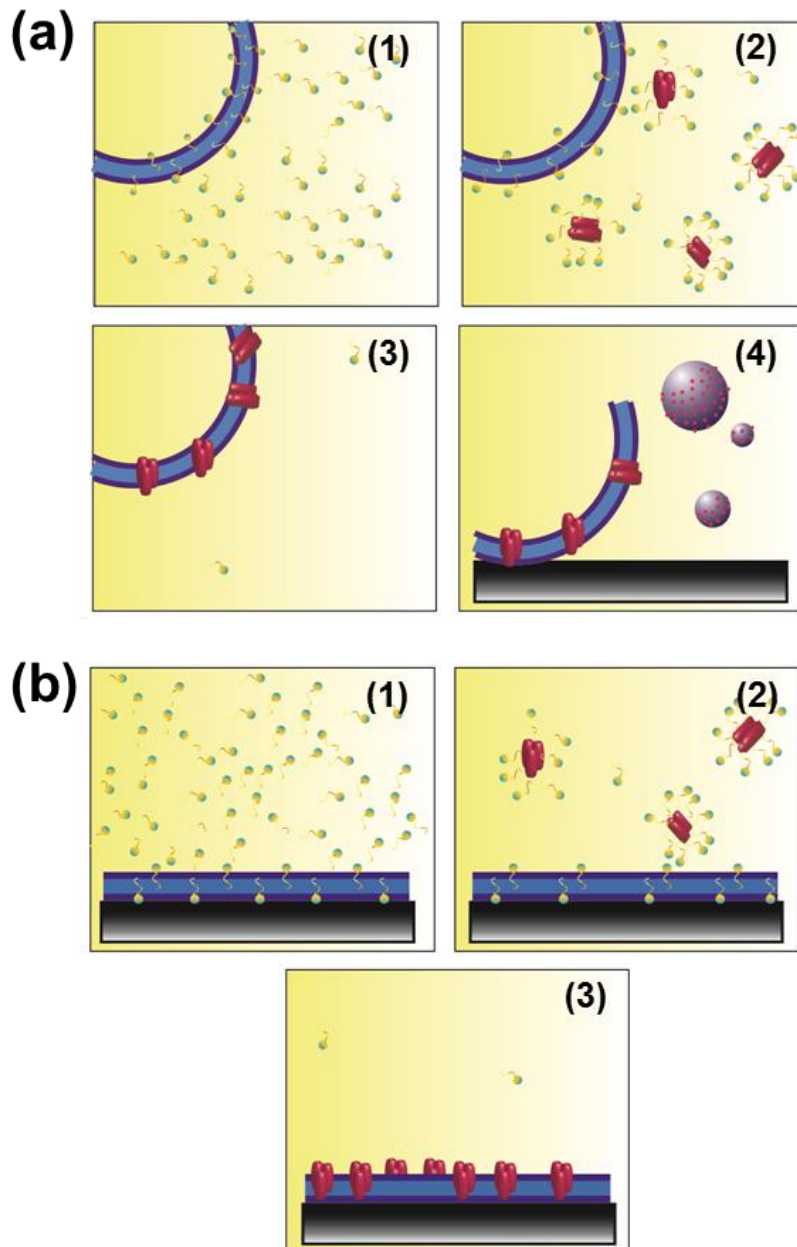
(b) Mixt-2: 4:3:1 POPC:POPE:POPG
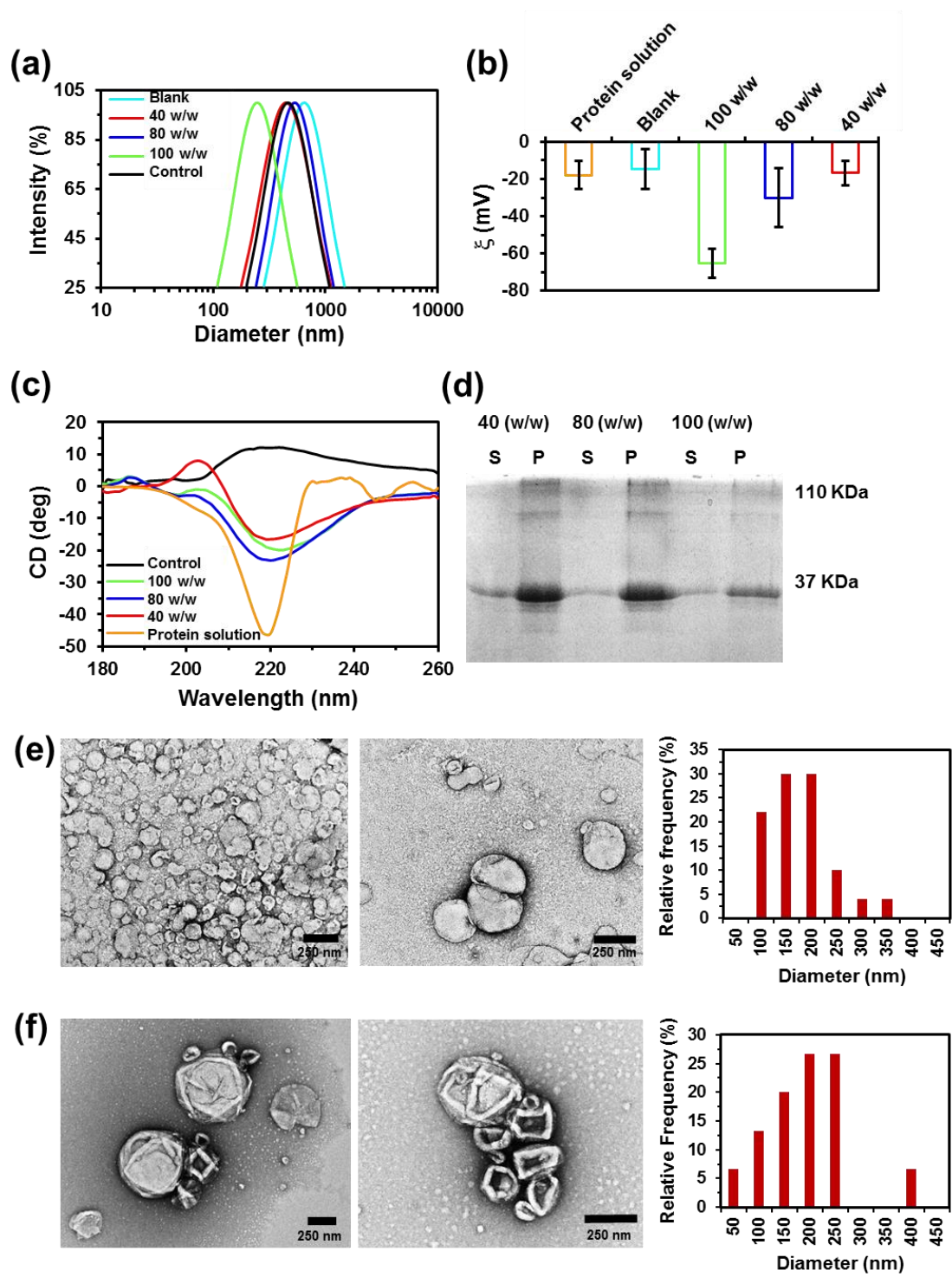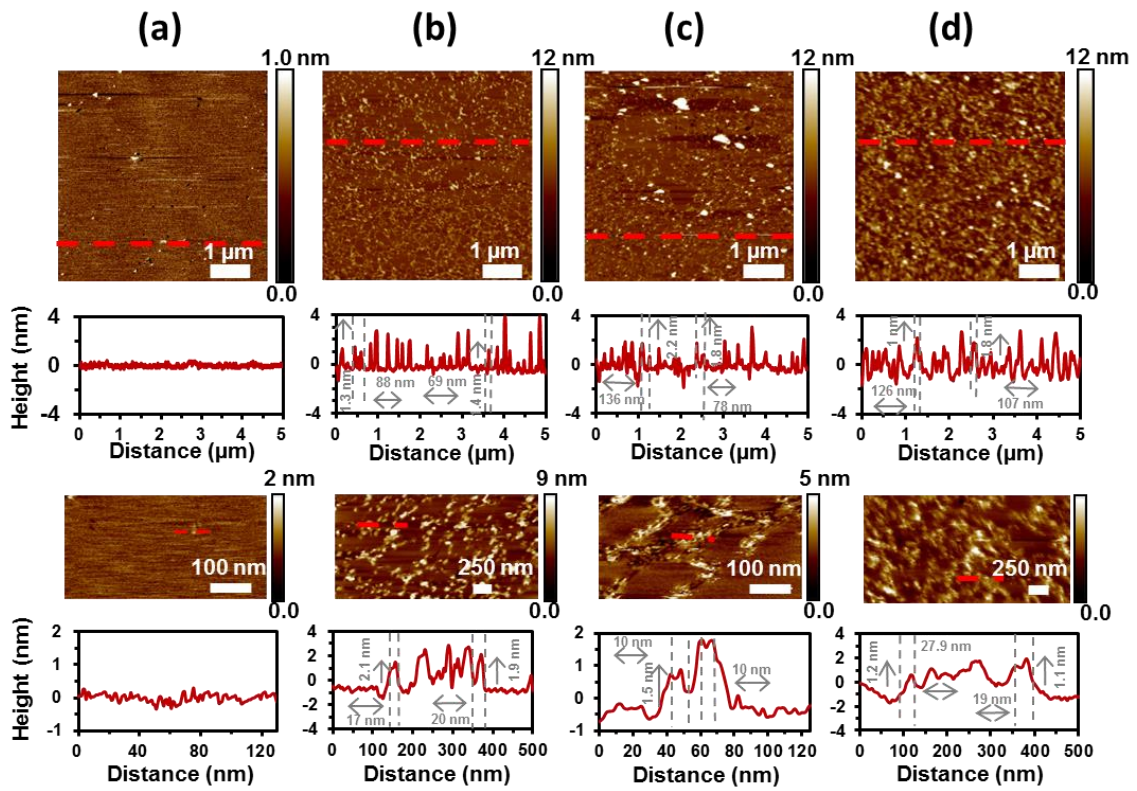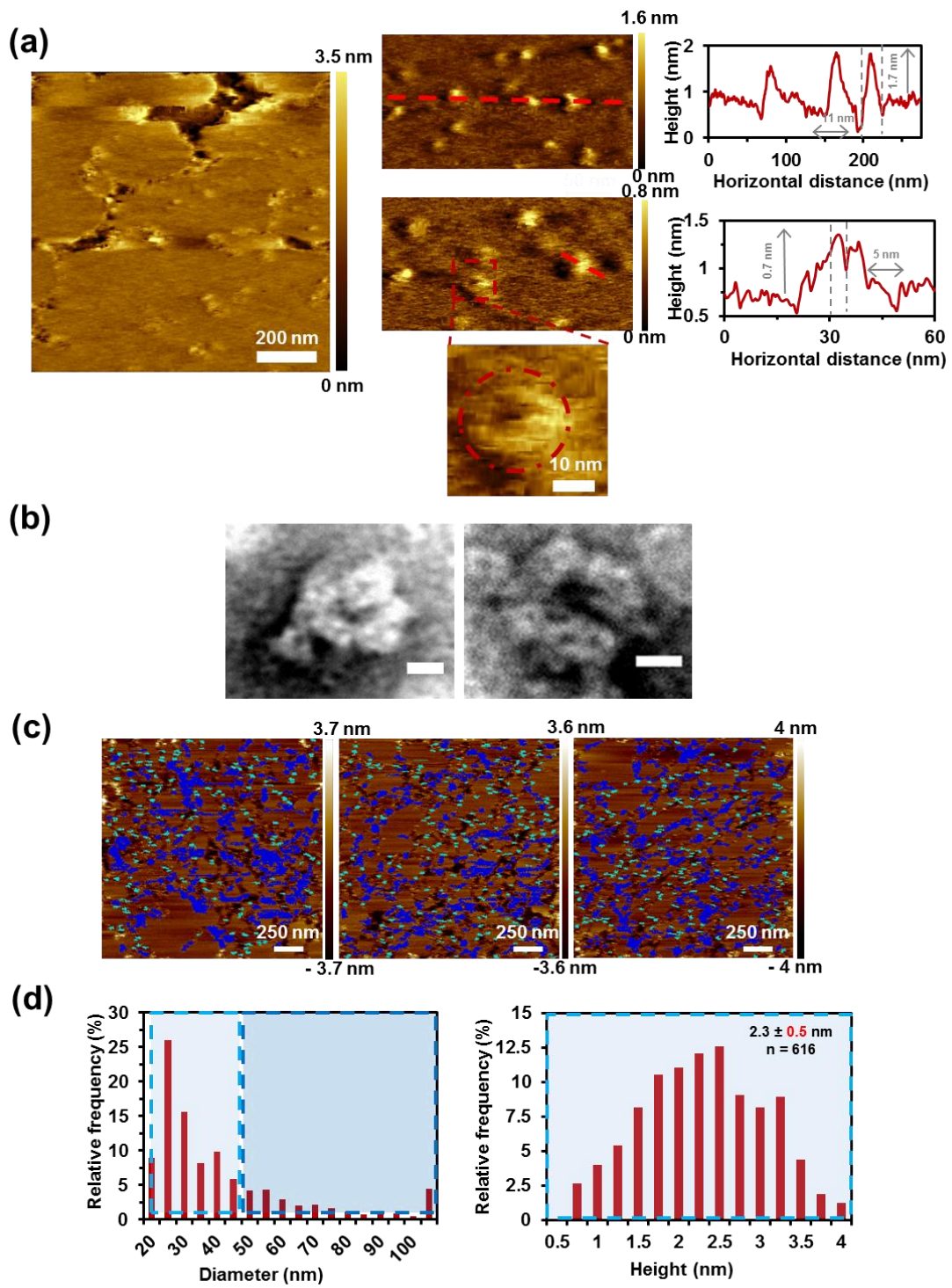
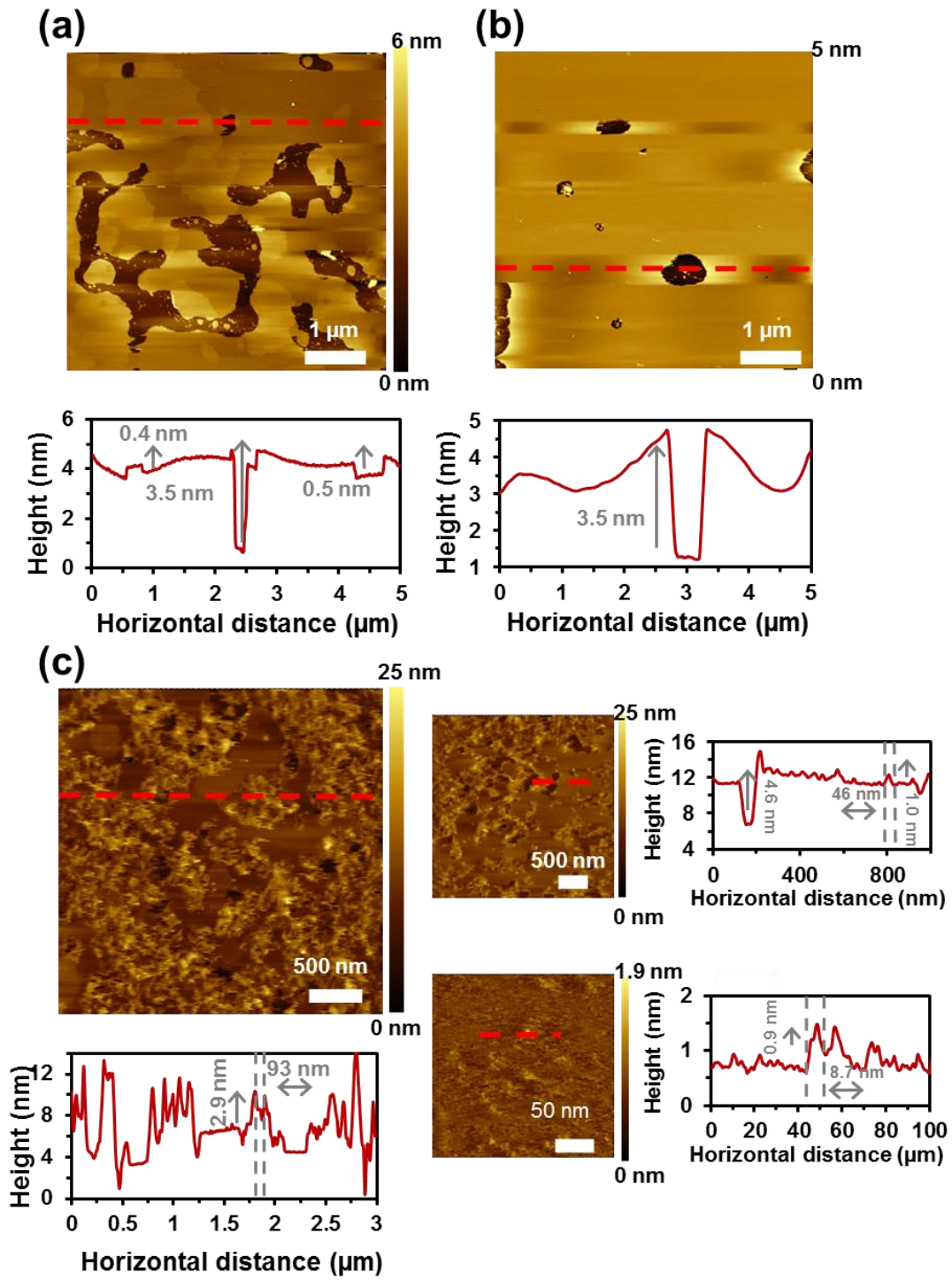**(c) Mixt-3: 4:3:1:2 POPC:POPE:POPG:CL**

Figure 1

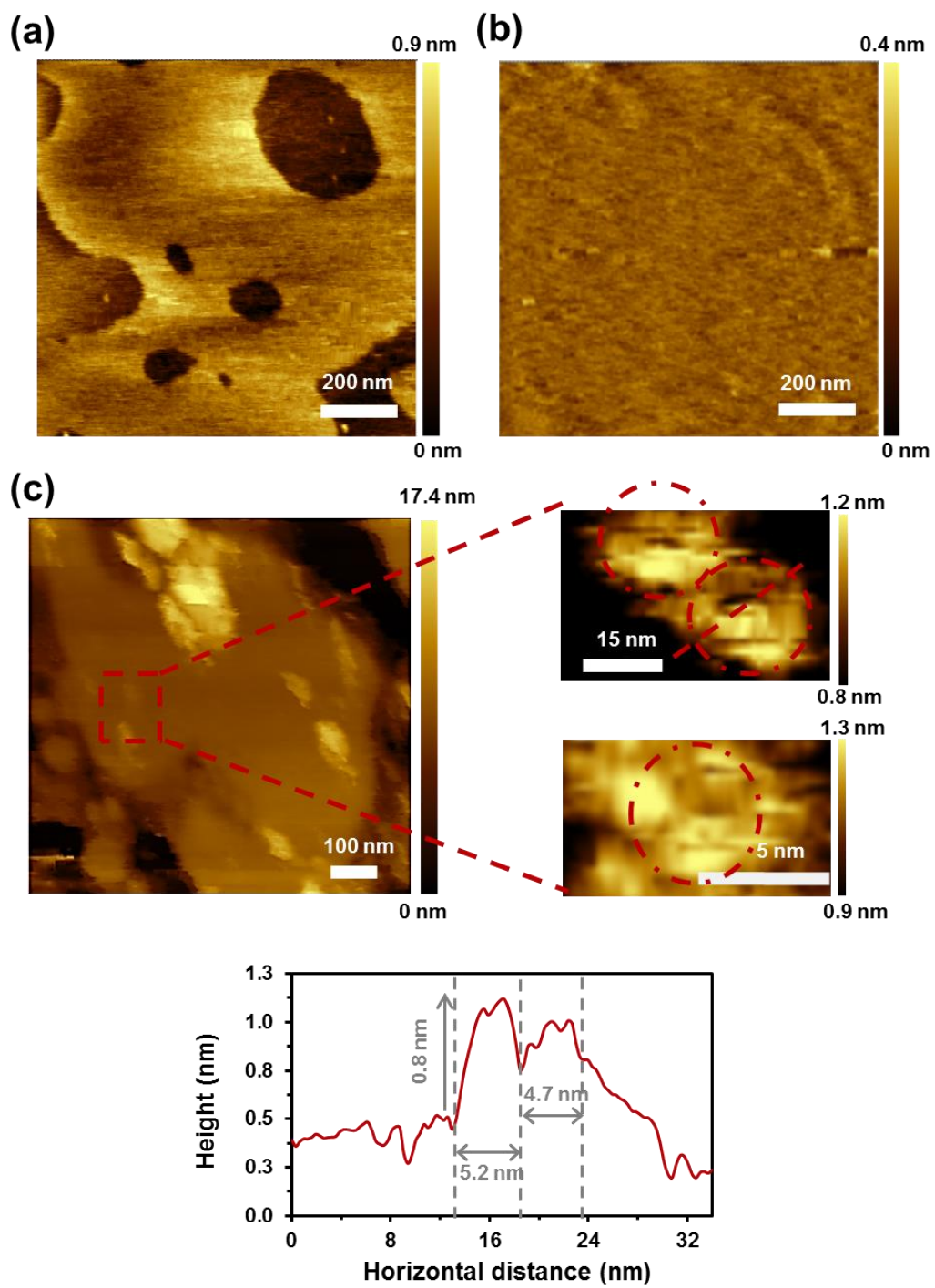Figure 2

Figure 3

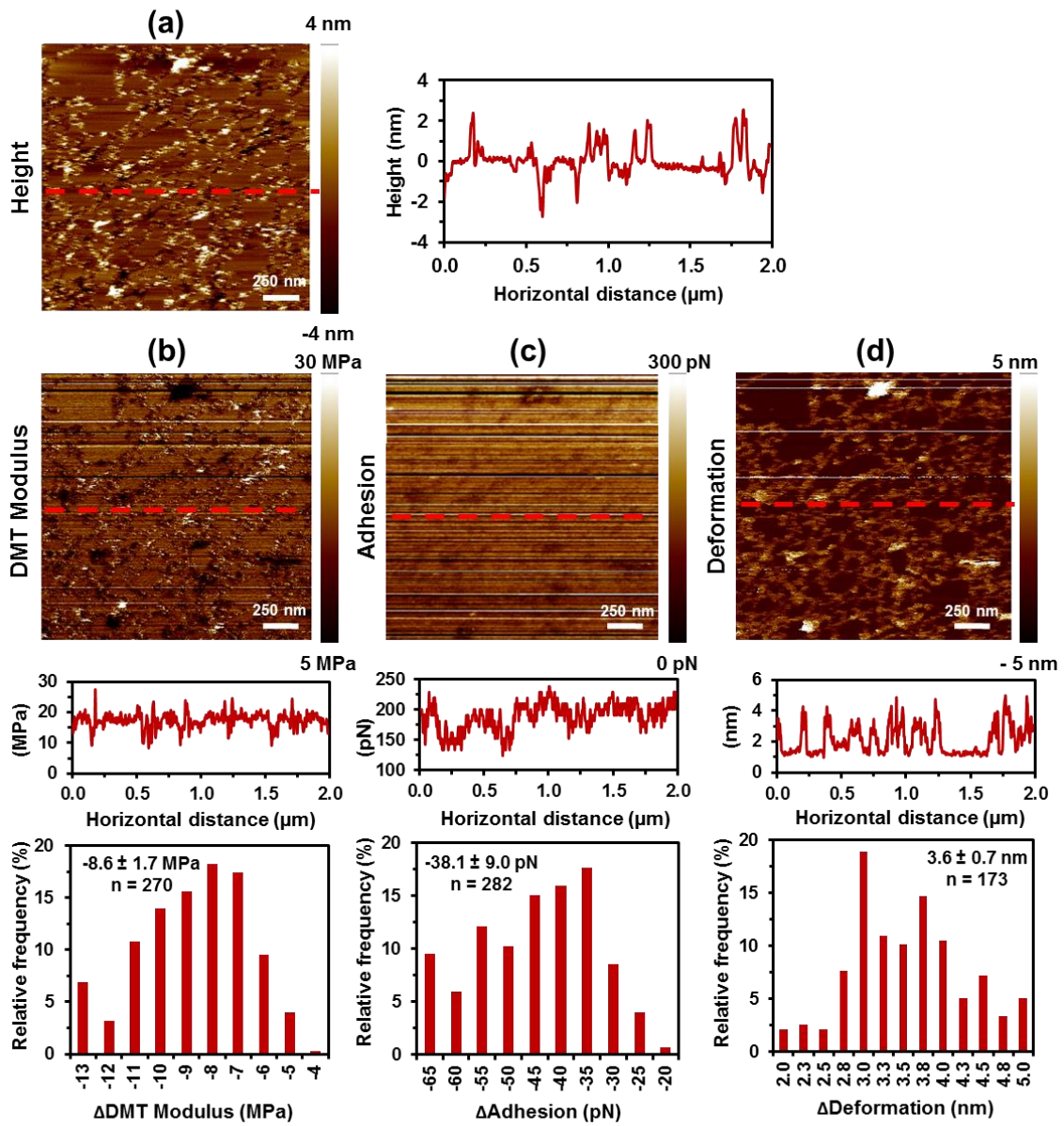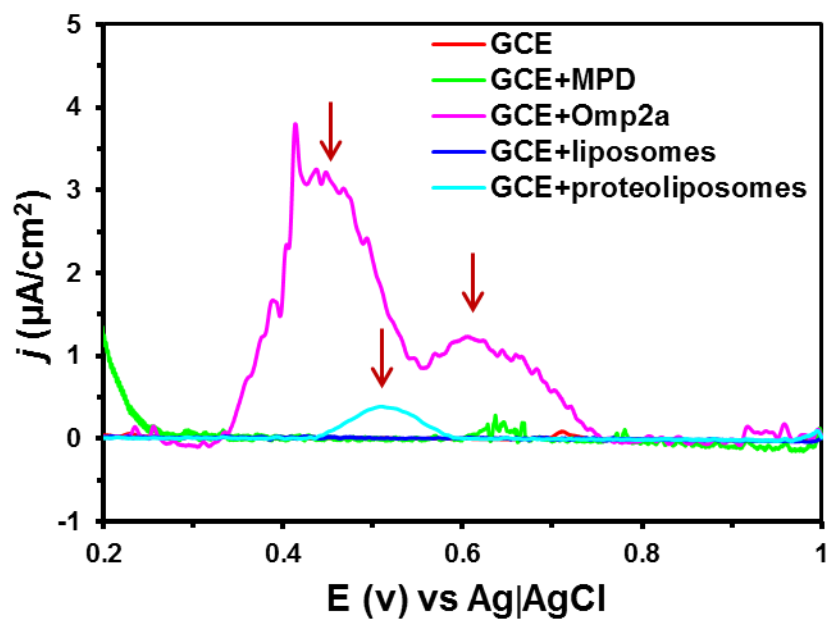Figure 4

Figure 5

Figure 6

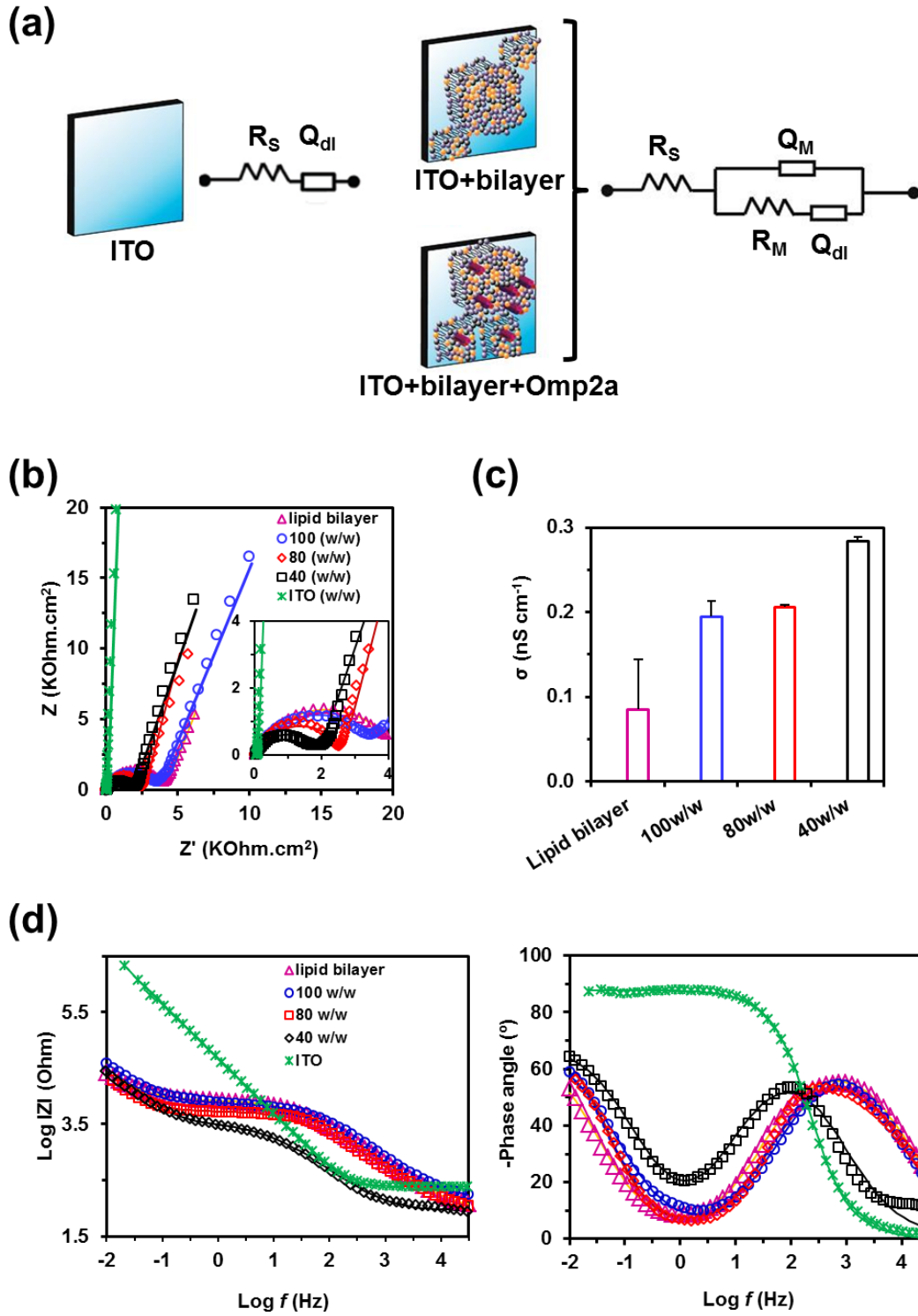Figure 7

Figure 8

Figure 9

Figure 10

Table 1. Resistances (R) and constant phase elements[a] (CPEs) for each sample, analyzed in KCl 0.1 M solution, from fitting parameters obtained with the EECs displayed in Figure 10a. The percentage error associated to each circuit element is included in parentheses.

	R_S ($\Omega \cdot cm^2$)	Q_M ($F \cdot cm^{-2} \cdot s^{n-1}$)	n	R_M ($K\Omega \cdot cm^2$)	Q_{dl} ($F \cdot cm^{-2} \cdot s^{n-1}$)	n
ITO	120.9 (0.6)	-	0.9 (0.5)	-	$6.9 \cdot 10^{-6}$ (0.1)	-
Lipid bilayer	44.7 (0.5)	$5.2 \cdot 10^{-6}$ (1.2)	0.7 (0.2)	4.2 (0.4)	$7.8 \cdot 10^{-4}$ (1.0)	0.8 (0.6)
Omp2a in SLB (100 w/w)	75.5 (3.3)	$4.2 \cdot 10^{-6}$ (1.2)	0.7 (1.2)	3.7 (1.9)	$4.5 \cdot 10^{-4}$ (3.4)	0.8 (1.9)
Omp2a in SLB (80 w/w)	43.8 (2.4)	$6.0 \cdot 10^{-5}$ (5.9)	0.7 (0.9)	2.7 (3.7)	$1.0 \cdot 10^{-3}$ (3.7)	0.8 (1.8)
Omp2a in SLB (40 w/w)	44.4 (2.2)	$3.2 \cdot 10^{-5}$ (8.1)	0.8 (1.6)	1.5 (3.8)	$6.3 \cdot 10^{-4}$ (3.6)	0.8 (2.2)

[a] The CPE impedances have been expressed as: $Z_{CPE} = [Q (j\omega)^n]^{-1}$. CPEs represent a capacitor and a resistor for n= 1 and n= 0, respectively, while it is associated with a diffusion process when n= 0.5.

REFERENCES

1. Jorest, T.; Klinger, A.; Gro, L. E.; Kawano, S.; Flinner, N.; Duchardt-Ferner, E.; Wöhnert, J.; Kalbacher, H.; Endo, T.; Schleiff, E.; Rapaport, D. Characterization of the Targeting Signal in Mitochondrial β-Barrel Proteins. *Nature Commun.* **2016**, *7*, 12036. DOI: 10.1038/ncomms12036

2. Saurel, O.; Iordanov, I.; Nars, G.; Demange, P.; Le Marchand, T.; Andreas, L. B.; Pintacuda, G.; Milon, A. Local and Global Dynamics in Klebsiella Pneumoniae Outer Membrane Protein a in Lipid Bilayers Probed at Atomic Resolution. *J. Am. Chem. Soc.* **2017**, *139*, 1590–1597. DOI: 10.1021/jacs.6b11565

3. Hwang, P. M.; Choy, W. Y.; Lo, E. I.; Chen, L.; Forman-Kay, J. D.; Raetz, C. R. H.; Prive, G. G.; Bishop, R. E.; Kay, L. E. Solution Structure and Dynamics of the Outer Membrane Enzyme PagP by NMR. *Proc. Natl. Acad. Sci.* **2002**, *99*, 13560–13565. DOI: 10.1073/pnas.212344499

4. Overington, J. P.; Al-Lazikani, B.; Hopkins, A. L. How Many Drug Targets Are There? *Nat. Rev. Drug Discovery* **2006**, *5*, 993−996. DOI: 10.1038/nrd2199

5. Koebnik, R.; Locher, K. P.; Van Gelder, P. Structure and Function of Bacterial Outer Membrane Proteins: Barrels in a Nutshell. *Mol. Microbiol.* **2000**, *37*, 239−253. DOI: 10.1046/j.1365-2958.2000.01983.x

6. Weeber, E. J.; Michael, L.; Sampson, M. J.; Anflous, K.; Armstrong, D. L.; Brown, S. E.; Sweatt, J. D.; Craigen, W. J. The Role of Mitochondrial Porins and the Permeability Transition Pore in Learning and Synaptic Plasticity. *J. Biol. Chem.* **2002**, *277*, 18891–18897. DOI: 10.1074/jbc.M201649200

7. Fischer, K.; Weber, A.; Brink, S.; Arbinger, B.; Schünemann, D.; Borchert, S.; Heldt, H. W.; Popp, B.; Benz, R.; Link, T. A.; Eckerskorn, C.; Flügge, U.-I. Porins from Plants – Molecular-Cloning and Functional-Characterization of 2 New Members of the Porin Family. *J. Biol. Chem.* **1994**, *269*, 25754–25760.

8. Shen, Y. X.; Saboe, P.; Sines, I. T.; Erbakan, M.; Kumar, M. Biomimetic Membranes: A review. *J. Membr. Sci.* **2014**, *454*, 359–381. DOI: 10.1016/j.memsci.2013.12.019

9. Kumar, M.; Grzelakowski, M.; Zilles, J.; Clark, M.; Meier, W. Highly Permeable Polymeric Membranes Based on the Incorporation of the Functional Water Channel Protein Aquaporin Z. *Proc. Natl. Acad. Sci. U. S. A.* **2007**, *104*, 20719−20724. DOI: 10.1073/pnas.0708762104

10. Gonzalez-Perez, A.; Stibius, K. B.; Vissing, T.; Nielsen, C. H.; Mouritsen, O. G. Biomimetic Triblock Copolymer Membrane Arrays: A Stable Template for Functional Membrane Proteins. *Langmuir* **2009**, *25*, 10447−10450. DOI: 10.1021/la902417m

11. Ali, M.; Nasir, S.; Nguyen, Q. H.; Sahoo, J. K.; Tahir, M. N.; Tremel, W.; Ensinger, W. Metal Ion Affinity-based Biomolecular Recognition and Conjugation inside Synthetic Polymer Nanopores Modified with Iron–Terpyridine Complexes. *J. Am. Chem. Soc.* **2011**, *133*, 17307−17314. DOI: 10.1021/ja205042t

12. Hou, X.; Guo, W.; Jiang, L. Biomimetic Smart Nanopores and Nanochannels. *Chem. Soc. Rev.* **2011**, *40*, 2385−2401. DOI: 10.1039/C0CS00053A

13. Pérez-Madrigal, M. M.; del Valle, L. J.; Armelin, E.; Michaux, C.; Roussel, G.; Perpète, E. A.; Alemán, C. Polypyrrole-Supported Membrane Proteins for Bio-Inspired Ion Channels. *ACS Appl. Mater. Interfaces* **2015**, *7*, 1632–1643. DOI: 10.1021/am507142f

14. Zhang, X.; Fu, W.; Palivan, C. G.; Meier, W. Natural Channel Protein Inserts and Functions in a Completely Artificial, Solid-Supported Bilayer Membrane. *Sci. Rep.* **2013**, *3*, 2196. DOI: 10.1038/srep02196

15. Hall, A. R.; Scott, A.; Rotem, D.; Mehta, K. K.; Bayley, H.; Dekker, C. Hybrid Pore Formation by Directed Insertion of [alpha]-Haemolysin into Solid-State Nanopores. *Nat. Nanotechnol.* **2010**, *5*, 874–877. DOI: 10.1038/nnano.2010.237

16. Balme, S.; Janot, J. M.; Berardo, L.; Henn, F.; Bonhenry, D.; Kraszewski, S.; Picaud, F.; Ramseyer, C. New Bioinspired Membrane Made of a Biological Ion Channel Confined into the Cylindrical Nanopore of a Solid-State Polymer. *Nano Lett.* **2011**, *11*, 712−716. DOI: 10.1021/nl103841m

17. Puiggalí-Jou, A., Pérez-Madrigal, M.M., del Valle, L.J., Armelin, E., Casas, M.T., Michaux, C., Perpète, E.A., Estrany, F., Alemán, C. Confinement of a β-Barrel Protein in Nanoperforated Free-Standing Nanomembranes for Ion Transport. *Nanoscale* **2016**, *8*, 16922–16935. DOI: 10.1039/C6NR04948F

18. Aguilella, V. M.; Queralt-Martín, M.; Aguilella-Arzo, M.; Alcaraz, A. . Insights on the Permeability of Wide Protein Channels: Measurement and Interpretation of Ion Selectivity. *Integr. Biol.* **2011**, *3*, 159–172. DOI: 10.1039/c0ib00048e

19. Moriyón, I.; López-Goñi, I. Structure and Properties of the Outer Membranes of Brucella Abortus and Brucella Melitensis. *Int. Microbiol.* **1998**, *1*, 19–26.

20. Uran, S.; Larsen, A.; Jacobsen, P. B.; Skotland, T. Analysis of Phospholipid Species in Human Blood Using Normal-Phase Liquid Chromatography Coupled with Electrospray Ionization Ion-Trap Tandem Mass Spectrometry. *J. Chromatogr. B. Biomed. Sci. Appl.* **2001**, *758*, 265–275. DOI: 10.1016/S0378-4347(01)00188-8

21. Leekumjorn, S.; Sum, A. K. Molecular Characterization of Gel and Liquid-Crystalline Structures of Fully Hydrated POPC and POPE Bilayers. *J. Phys. Chem. B* **2007**, *111*, 6026–6033. DOI: 10.1021/jp0686339

22. Unsay, J. D.; Cosentino, K.; Subburaj, Y.; García-Sáez, A. J. Cardiolipin Effects on Membrane Structure and Dynamics. *Langmuir* **2013**, *29*, 15878–15887. DOI: 10.1021/la402669z

23. Li, Z.; Ma, J.; Lee, N. S.; Wooley, K. L. Dynamic Cylindrical Assembly of Triblock Copolymers by a Hierarchical Process of Covalent and Supramolecular Interact. *J. Am. Chem. Soc.* **2011**, *133*, 1228–1231. DOI: 10.1021/ja109191z

24. Yan, Q.; Yuan, J.; Cai, Z.; Xin, Y.; Kang, Y.; Yin, Y. Voltage-Responsive Vesicles Based on Orthogonal Assembly of Two Homopolymers. *J. Am. Chem. Soc.* **2010**, *132*, 9268–9270. DOI: 10.1021/ja1027502

25. Yan, Q.; Zhou, R.; Fu, C.; Zhang, H.; Yin, Y.; Yuan, Y. CO_2-Responsive Polymeric Vesicles that Breathe. *Angew. Chem., Int. Ed.* **2011**, *50*, 4923–4927. DOI: 10.1002/anie.201100708

26. Willumeit, R.; Kumpugdee, M.; Funari, S. S.; Lohner, K.; Pozo-Navas, B.; Brandenburg, K.; Linser, S.; Andrä, J. Structural Rearrangement of Model Membranes by the Peptide Antibiotic NK-2. *Biochim. Biophys. Acta - Biomembr.* **2005**, *1669*, 125–134. DOI: 10.1016/j.bbamem.2005.01.011

27. Zeczycki, T. N.; Whelan, J.; Hayden, W. T.; Brown, D.; Shaikh, S. R. Increasing Levels of Cardiolipin Differentially Influence Packing of Phospholipids Found in the Mitochondrial Inner Membrane. *Biochem. Biophys. Res. Commun.* **2014**, *450*, 366–371. DOI: 10.1016/j.bbrc.2014.05.133

28. Rigaud, J. L.; Pitard, B.; Levy, D. Reconstitution of Membrane Proteins into Liposomes: Application to Energy-Transducing Membrane Proteins. *Biochim. Biophys. Acta - Bioenerg.* **1995**, *1231*, 223–246. DOI: 10.1016/0005-2728(95)00091-V

29. Geertsma, E. R.; Nik Mahmood, N. A.; Schuurman-Wolters, G. K.; Poolman, B. Membrane Reconstitution of ABC Transporters and Assays of Translocator Function. *Nat. Protoc.* **2008**, *3*, 256–266. DOI: 10.1038/nprot.2007.519

30. Seddon, A. M.; Curnow, P.; Booth, P. J. Membrane Proteins, Lipids and Detergents: Not Just a Soap Opera. *Biochim. Biophys. Acta - Biomembr.* **2004**, *1666*, 105–117. DOI: 10.1016/j.bbamem.2004.04.011

31. Rigaud, J.; Levy, D. Reconstiution of Membrane Proteins into Liposomes. *Methods Enzymol.* **2003**, *372*, 65–86. DOI: 10.1016/S0076-6879(03)72004-7

32. Santos, H. J.; Imai, K.; Makiuchi, T.; Tomii, K.; Horton, P.; Nozawa, A.; Ibrahim, M.; Tozawa, Y.; Nozaki, T. A Novel Mitosomal β-Barrel Outer Membrane Protein in Entamoeba. *Sci. Rep.* **2015**, *5*, 8545. DOI: 10.1038/srep08545

33. Opaliński, Ł.; Kiel, J. A. K. W.; Williams, C.; Veenhuis, M.; van der Klei, I. J. Membrane Curvature During Peroxisome Fission Requires Pex11. *EMBO J.* **2011**, *30*, 5–16. DOI: 10.1038/emboj.2010.299

34. Leonenko, Z. V.; Carnini, A.; Cramb, D. T. Supported Planar Bilayer Formation by Vesicle Fusion: The Interaction of Phospholipid Vesicles with Surfaces and the Effect of Gramicidin on Bilayer Properties Using Atomic Force Microscopy. *Biochim. Biophys. Acta - Biomembr.* **2000**, *1509*, 131–147. DOI: 10.1016/S0005-2736(00)00288-1

35. Richter, R.; Mukhopadhyay, A.; Brisson, A. Pathways of Lipid Vesicle Deposition on Solid Surfaces: A Combined QCM-D and AFM Study. *Biophys. J.* **2003**, *85*, 3035–3047. DOI: 10.1016/S0006-3495(03)74722-5

36. Berquand, A.; Lévy, D.; Gubellini, F.; Le Grimellec, C.; Milhiet, P. E. Influence of Calcium on Direct Incorporation of Membrane Proteins into In-Plane Lipid Bilayer. *Ultramicroscopy* **2007**, *107*, 928–933. DOI: 10.1016/j.ultramic.2007.04.008

37. Maire, M. L.; Champeil, P.; Möller, J. V. Interaction of Membrane Proteins and Lipids with Solubilizing Detergents. *Biochim. Biophys. Acta* **2000**, *1508*, 86–111. DOI: 10.1016/S0304-4157(00)00010-1

38. Milhiet, P.-E.; Gubellini, F.; Berquand, A.; Dosset, P.; Rigaud, J. L.; Le Grimellec, C.; Levy, D. High-Resolution AFM of Membrane Proteins Directly Incorporated at High Density in Planar Lipid Bilayer. *Biophys. J.* **2006**, *91*, 3268–3275. DOI: 10.1529/biophysj.106.087791

39. Sumino, A.; Uchihashi, T.; Oiki, S. Oriented Reconstitution of the Full-Length KcsA Potassium Channel in a Lipid Bilayer for AFM Imaging. *J. Phys. Chem. Lett.* **2017**, *8*, 785–793. DOI: 10.1021/acs.jpclett.6b03058

40. Chada, N.; Sigdel, K. P.; Reddy, R.; Gari, S.; Matin, T. R.; Randall, L. R.; King, G. M. Glass is a Viable Substrate for Precision Force Microscopy of Membrane Proteins. *Sci. Rep.* **2015**, *5*, 12550. DOI: 10.1038/srep12550

41. Lü, J.; Yang, J.; Dong, M.; Sahin, O. Nanomechanical Spectroscopy of Synthetic and Biological Membranes. *Nanoscale* **2014**, *6*, 7604–7608. DOI: 10.1039/C3NR02643D

42. Lingwood, D.; Simons, K. Lipid Rafts as a Membrane-Organizing Principle. *Science* **2010**, *327*, 46–50. DOI: 10.1126/science.1174621

43. Voss, A.; Dietz, C.; Stocker, A.; Stark, R. W. Quantitative Measurement of the Mechanical Properties of Human Antibodies with Sub-10-nm Resolution in a Liquid Environment. *Nano Res.* **2015**, *8*, 1987–1996. DOI: 10.1007/s12274-015-0710-5

44. Saphire, E. O.; Stanfield, R. L.; Crispin, M. D.; Parren, P. W.; Rudd, P. M.; Dwek, R. A.; Burton, D. R.; Wilson, I. A. Contrasting IgG Structures Reveal Extreme Asymmetry and Flexibility. *J. Mol. Biol.* **2002**, *319*, 9–18. DOI: 10.1016/S0022-2836(02)00244-9

45. Freundschuh, M.; Martinez-Martin, D.; Mulvihill, E.; Wegmann, S.; Muller, D. J. Multiparametric High-Resolution Imaging of Native Proteins by Force-Distance Curve-Based AFM. *Nat. Protoc.* **2014**, *9*, 1113–1130. DOI: 10.1038/nprot.2014.070

46. Derjaguin, B. V.; Muellen, V. M.; Toporov, Y. P. Effect of Contact Deformations on the Adhesion of Particles. *J. Colloid Interface Sci.* **1975**, *53*, 314–326. DOI: 10.1016/0021-9797(75)90018-1

47. Mari, S. A.; Köster, S.; Bippes, C. A.; Yildiz, Ö.; Kühlbrandt, W.; Muller, D. J. pH-Induced Conformational Change of the β-Barrel-Forming Protein OmpG Reconstituted into Native E. coli Lipids. *J. Mol. Biol.* **2010**, *396*, 610–616. DOI: 10.1016/j.jmb.2009.12.034

48. Medalsy, I. D.; Muller, D. J. Nanomechanical Properties of Proteins and Membranes Depend on Loading Rate and Electrostatic Interactions. *ACS Nano* **2013**, *7*, 2642–2650. DOI: 10.1021/nn400015z

49. Dong, M.; Husale, S.; Sahin, O. Determination of Protein Structural Flexibility by Microsecond Force Spectroscopy. *Nat. Nanotechnol.* **2009**, *4*, 514–517. DOI: 10.1038/nnano.2009.156

50. Picas, L.; Rico, F.; Deforet, M.; Scheuring, S. Structural and Mechanical Heterogeneity of the Erythrocyte Membrane Reveals Membrane Stability. *ACS Nano* **2013**, *7*, 1054–1063. DOI: 10.1021/nn303824j

51. Sullan, R. M.; Li, J. K.; Zou, S. Direct Correlation of Structures and Nanomechanical Properties of Multicomponent Lipid Bilayers. *Langmuir* **2009**, *25*, 7471–7477. DOI: 10.1021/la900395w

52. Li, J. K.; Sullan, R. M.; Zou, S. Atomic Force Microscopy Force Mapping in the Study of Supported Lipid Bilayers. *Langmuir* **2011**, *27*, 1308–1313. DOI: 10.1021/la103927a

53. Konarzewska, D.; Juhaniewicz, J.; Guzeloglu, A.; Sek, S. Characterization of Planar Biomimetic Lipid Films Composed of Phosphatidylethanolamines and Phosphatidylglycerols from Escherichia Coli. *Biochim. Biophys. Acta* **2017**, *1859*, 475–483. DOI: 10.1016/j.bbamem.2017.01.009

54. Pérez-Madrigal, M.; Giannoti, M. I.; Oncins, G.; Franco, L.; Armelin, E.; Puiggalí, J.; Sanz, F.; del Valle, L. J.; Alemán, C. Bioactive Nanomembranes of Semiconductor Polythiophene and Thermoplastic Polyurethane: Thermal, Nanostructural and Nanomechanical Properties. *Polym. Chem.* **2013**, *4*, 568–583. DOI: 10.1039/C2PY20654D

55. Lin, D. C.; Dimitriadis, E. K. Robust Strategies for Automated AFM Force Curve Analysis-Ii: Adhesion-Influenced Indentation of Soft, Elastic Materials. *J. Biomech. Eng.* **2007**, *129*, 904–912. DOI: 10.1115/1.2800826

56. Medalsy, I.; Hensen, U.; Muller, D. J. Imaging and Quantifying Chemical and Physical Properties of Native Proteins at Molecular Resolution by Force-Volume AFM. *Angew. Chemie - Int. Ed.* **2011**, *50*, 12103–12108. DOI: 10.1002/anie.201103991

57. Ostatná, V.; Černocká, H.; Kurzatkowska, K.; Paleček, E. Native and Denatured Forms of Proteins Can Be Discriminated At edge Plane Carbon Electrodes. *Anal. Chim. Acta* **2012**, *735*, 31–36. DOI: 10.1016/j.aca.2012.05.012

58. Brabec, V. Electrochemical Oxidation of Nucleic Acids and Proteins at Graphite Electrode. Qualitative Aspects. *J. Electroanal. Chem. Interfacial Electrochem.* **1979**, *116*, 69–82. DOI: 10.1016/S0022-0728(80)80222-1

59. Paleček, E.; Tkác, J.; Bartošík, M.; Bertók, T.; Ostatná, V.; Paleček, J. Electrochemistry of Nonconjugated Proteins and Glycoproteins. Toward Sensors for Biomedicine and Glycomics. *Chem. Rev.* **2015**, *115*, 2045–2108. DOI: 10.1021/cr500279h

60. Paleček, E.; Jelen, F.; Teijeiro, V.; Fučík, T. M. Biopolymer-Modified Electrodes in the Voltammetric Determination of DNA and Protein at the Submicrogram Level. *Anal. Chim. Acta* **1993**, 273, 175–186. DOI: 10.1016/0003-2670(93)80156-F

61. Vacek, J.; Vrba, J.; Zatloukalová, M.; Kubala, M. Electrochemical Oxidation of Proteins Using Ionic Liquids as Solubilizers, Adsorption Solvents and Electrolytes. *Electrochim. Acta* **2014**, *126*, 31–36. DOI: 10.1016/j.electacta.2013.06.115

62. Hille, B. Ligand gated channels of fast chemical synapses. In Ion Channels of Excitable Membranes, 3rd ed.; Sinauer Associates: Sunderland, MA, 2001; pp 169-200.

63. Fyles, T. M. Synthetic Ion Channels in Bilayer Membranes. *Chem. Soc. Rev.* **2007**, *36*, 335−347. DOI: 10.1039/B603256G

64. Kumar, M.; Grzelakowski, M.; Zilles, J.; Clark, M.; Meier, W. Highly Permeable Polymeric Membranes Based on the Incorporation of the Functional Water Channel

Protein Aquaporin Z. *Proc. Natl. Acad. Sci. U. S. A.* **2007**, *104*, 20719−20724. DOI: 10.1073/pnas.0708762104

65. Ali, M.; Ramirez, P.; Mafe, S.; Neumann, R.; Ensinger, W. A pH-Tunable Nanofluidic Diode with a Broad Range of Rectifying Properties. *ACS Nano* **2009**, *3*, 603−608. DOI: 10.1021/nn900039f

66. Cao, L. X.; Guo, W.; Ma, W.; Wang, L.; Xia, F.; Wang, S. T.; Wang, Y. G.; Jiang, L.; Zhu, D. B. Towards Understanding the Nanofluidic Reverse Electrodialysis System: Well Matched Charge Selectivity and Ionic Composition. *Energy Environ. Sci.* **2011**, *4*, 2259−2266. DOI: 10.1039/C1EE01088C

67. Vlassiouk, I.; Apel, P. Y.; Dmitriev, S. N.; Healy, K.; Siwy, Z. S. Versatile Ultrathin Nanoporous Silicon Nitride Membranes. *Proc. Natl. Acad. Sci. U. S. A.* **2009**, *106*, 21039−21044. DOI: 10.1073/pnas.0911450106

68. Kim, S.; Nham, J.; Jeong, Y. S.; Lee, C. S.; Ha, S. H.; Park, H. B.; Lee, Y. J. Biomimetic Selective Ion Transport through Graphene Oxide Membranes Functionalized with Ion Recognizing Peptides. *Chem. Mater.* **2015**, *27*, 1255−1261. DOI: 10.1021/cm504212j

69. Gritsch, S.; Nollert, P.; Jähnig, F.; Sackmann, E. Impedance Spectroscopy of Porin and Gramicidin Pores Reconstituted into Supported Lipid Bilayers on Indium−Tin−Oxide Electrodes. *Langmuir*, **1998**, *14*, 3118–3125. DOI: 10.1021/la9710381

70. Hillebrandt, H.; Wiegand, G.; Tanaka, M.; Sackmann, E. High Electric Resistance Polymer / Lipid Composite Films on Indium−Tin−Oxide Electrodes. *Langmuir* **1999**, *15*, 8451–8459. DOI: 10.1021/la990341u

71. Lin, J.; Motylinski, J.; Krauson, A. J.; Wimley, W. C.; Searson, P. C.; Hristova, K. Interactions of Membrane Active Peptides with Planar Supported Bilayers: An Impedance Spectroscopy Study. *Langmuir* **2012**, *28*, 6088–6096. DOI: 10.1021/la300274n

72. Wiegand, G.; Arribas-layton, N.; Hillebrandt, H.; Sackmann, E.; Wagner, P. Electrical Properties of Supported Lipid Bilayer Membranes. *J. Phys. Chem. B* **2002**, *106*, 4245–4254. DOI: 10.1021/jp014337e

73. Juhaniewicz, J.; Sek, S. Atomic Force Microscopy and Electrochemical Studies of Melittin Action on Lipid Bilayers Supported on Gold Electrodes. *Electrochim. Acta* **2015**, *162*, 53–61. DOI: 10.1016/j.electacta.2014.10.039

For Table of Contents Only